Title: Pangenomics facilitated with structural analysis reveals host NAD^+ manipulation as a major virulence activity of bacterial effectors

Short title: Bacterial effectors manipulate NAD^+

Michelle T Hulin[1], Wenbo Ma[1*]

[1] The Sainsbury Laboratory, Norwich Research Park, NR4 7UH, United Kingdom

[*] Corresponding author: wenbo.ma@tsl.ac.uk

The author(s) responsible for distribution of materials integral to the findings presented in this article in accordance with the policy described in the Instructions for Authors is: wenbo.ma@tsl.ac.uk

Abstract (200 words)

Nicotinamide adenine dinucleotide (NAD^+) has emerged as a major component in both eukaryotic and prokaryotic immune systems. Recent findings that Toll/interleukin-1 receptor (TIR) proteins function as NAD^+ hydrolases (NADase) link NAD^+ metabolism with immune signaling. In this study, we investigated how manipulation of host NAD^+ metabolism can be employed as a virulence strategy by pathogens. Using the pangenome of the model bacterial pathogen *Pseudomonas syringae*, we conducted a structure-based similarity search for type III effectors (T3Es) with potential NADase activity from 35,000 orthogroups. Thirteen T3Es, including five novel ones, were identified to possess domain(s) related to seven NAD^+-hydrolyzing enzyme families. Most *P. syringae* strains encode at least one NAD^+-manipulating T3Es, and many have multiple. We experimentally confirmed the type III-dependent secretion and virulence activity of a novel T3E, which shows similarity with both TIR and adenosine diphosphate ribose (ADPR) cyclase. Using AI-based structural prediction and *in silico* molecular docking, we found divergence at the NAD^+-interacting positions and confirmed the functional importance of these residues in the TIR T3E HopAM1. This study highlights NAD^+ manipulation as a key virulence mechanism and provides insights into how pathogens may promote infection through manipulation of host NAD^+ metabolism.

Introduction

The metabolite and redox agent nicotinamide adenine dinucleotide (NAD^+) is a universal co-factor and essential redox carrier involved in diverse cellular processes. Recently research on the Toll/Interleukin-1 receptor (TIR) domain proteins has established a central role of NAD^+ in immune signaling across the kingdoms. TIR proteins were first identified as a stretch of ~150 conserved amino acids shared between Toll and Interleukin immune receptors in animals (Gay and Keith, 1991). TIR domains often associate with other domains that sense the presence of pathogens. Upon activation, TIR proteins cleave NAD^+ through a N-glycosidase activity (Essuman et al., 2017; Ofir et al., 2021; Wan et al., 2019), producing adenosine diphosphate ribose (ADPR) and nicotinamide (NAM). TIR proteins can also have cyclase activity to produce cyclic ADPR (cADPR) or variants of cADPR (v-cADPR), as well as base-exchange activity to produce nicotinic acid adenine dinucleotide (NAAD) (Angeletti et al., 2022). All these enzymatic activities are dependent on a catalytic Glutamic acid (Glu) within the catalytic site (Burdett et al., 2021; Duxbury et al., 2020). The resulting NAD^+-derived molecules activate immune signaling and in some cases metabolite depletion leads directly to cell death (Ofir et al., 2021).

In plants, the TIR domain is often associated with intracellular immune receptors that also contain the nucleotide binding/leucine-rich repeat (NLR) domains (Kourelis and van der Hoorn, 2018). The NLR proteins have been evolved to sense pathogen effectors, which are secreted to promote disease. TIR-NLR-triggered immunity is usually dependant on downstream Enhanced Disease Susceptibility 1 (EDS1)-helper NLR pathways (Adlung et al., 2016). Plant TIRs produce various products, including ADPR, NAM and a v-cADPR (Table 1), through NAD^+ hydrolysis (Huang et al., 2022; Jia et al., 2022; Ma et al., 2020; Wan et al., 2019). The structure of v-cADPR was recently identified as an isomer of cADPR and renamed 2'-cADPR (Manik et al., 2022). Other TIR generated products pRib-AMP/ADP, ADPR-ATP and diADPR were shown to bind to and activate specific EDS1 heterodimers (Huang et al., 2022; Jia et al., 2022), indicating these small molecules link TIR activation to EDS1-dependant immune signalling. In addition, TIR-only proteins also exhibit 2',3'-cNMP synthase

activity *in vitro* and these cyclic nucleotides may also contribute to immunity (Yu et al., 2022).

With the establishment of NAD^+ metabolism as a major theme in innate immunity, it is intuitive to speculate that this process is manipulated by pathogens as a virulence strategy. For example, sequestering/degrading small molecule signals to block downstream signaling, or competing for the NAD^+ substrate to generate distinct molecules. Indeed, Tad1 produced by bacteriophages binds to a TIR-produced small molecule as a sponge to interfere with bacterial anti-viral defence (Leavitt et al., 2022). Intriguingly, pathogens can also suppress immunity using TIR effectors. BtpA and BtpB produced by the animal pathogen *Brucella abortus* reduce host NAD^+ levels to promote infection (Coronas-Serna et al., 2020). The type III effector (T3E) HopAM1 produced by the plant pathogen *Pseudomonas syringae* cleaves NAD^+ and produces 3'-cADPR (originally designated v2-cADPR), which differs from the 2'-cADPR produced by characterised plant TIR proteins (Eastman et al., 2022; Manik et al., 2022).

Apart from the TIR proteins, there are additional enzymes that can cleave NAD^+ at either the pyrophosphate bond or the N-glycosidic bond by multiple enzymes (Figure 1; Table 1). The NUDIX (nucleoside diphosphate linked to a variable moiety X) pyrophosphatase enzymes (Srouji et al., 2017) and phosphodiesterases (PDEs) cleave pyrophosphate bonds. Pathogen effector proteins harboring the NUDIX domain include the oomycete pathogen *Phytophthora sojae* effector Avr3b, which hydrolyses NADH, ADPR as well as 2',3'-cNMPs (Dong et al., 2011; Yu et al., 2022) and the *Ralstonia solanacearum* T3E RipN, which alters the NAD+/NADH ratio to dampen immune responses (Sun et al., 2019). The PDE superfamily contains diverse groups with various functions, structures and different catalytic mechanisms (Azevedo et al., 2014). An example of PDE effector is SdeA produced by the animal bacterial pathogen *Legionella pneumophila* (Akturk et al., 2018).

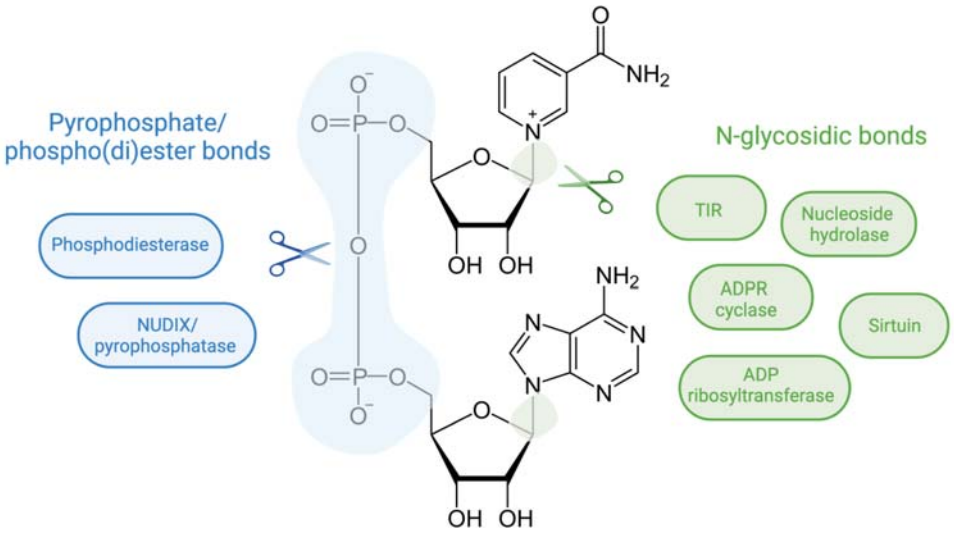

Figure 1. Enzyme families that may hydrolyse NAD⁺.
The NUDIX (nucleoside diphosphate linked to a variable moiety X) enzymes and phosphodiesterases (PDEs) cleave the pyrophosphate bond. ADP-ribosyltransferases (ART), nucleoside hydrolases (NH), ADPR cyclases, and sirtuins cleave the N-glycosidic bond.

Enzymes that can potentially cleave the N-glycosidic bond in NAD^+ include ADP-ribosyltransferases (ART), nucleoside hydrolases (NH), ADPR cyclases, and sirtuins (Figure 1). ARTs cleave NAD^+ to release ADPR for post-translational modifications of proteins and nucleic acids (Corda and Di Girolamo, 2003; Takamura-Enya et al., 2001). However, some ARTs act primarily as NAD^+ glycohydrolases and don't require a protein substrate (Ghosh and Caparon, 2006). ART effectors have been identified in various pathogens although most of them are presumed to modify host protein targets (Schreiber et al., 2021). A nucleoside hydrolase effector is the *P. syringae* T3E HopQ1, which was shown to alter purine metabolism (Li et al., 2013) and activate cytokinin signaling by hydrolyzing the cytokinin precursor iP-riboside 5′-monophosphate (iPRMP) (Hann et al., 2014; Li et al., 2013). Sirtuins utilise NAD^+ as a co-factor during protein deactylation (Sanders et al., 2010); however, the sirtuin ThsA in *Bacillus cereus* primarily acts to deplete NAD^+ during anti-viral immunity (Ofir et al., 2021). Finally, ADPR cyclases have similar activity to TIR proteins to cleave NAD^+ into ADPR, cADPR and NAM, despite limited sequence similarity (Lee

115 and Zhao, 2019). So far, pathogen effectors with sirtuin or ADPR cyclase domains
116 have not been identified.
117
118 Here, we employ pangenomic and structure-based similarity searches to identify
119 effectors with potential NADase activity from the model bacterial pathogen *P.*
120 *syringae*. We found *P. syringae*, as a species complex, has a diverse T3E repertoire
121 with various enzymatic activities that may hydrolyze NAD^+, supporting that
122 manipulation of NAD^+ metabolism is a key virulence mechanism. Furthermore, we
123 examined the structural features of the *P. syringae* TIR proteins using AlphaFold2
124 and *in silico* docking. This analysis revealed diversity at the NAD^+-interacting
125 residues, which may fine tune the enzymatic activities, thus providing insight into
126 how effectors may promote infection through NAD^+ manipulation in the host.
127
128

Results

Pangenome analysis of putative NADases in *P. syringae*

Traditionally classified into pathovars based on host of isolation, *P. syringae* is a species complex infecting over 180 different plant species (Young, 2010). Utilizing the pangenomic diversity of *P. syringae*, we systematically analyzed NADase-encoding proteins using pipelines illustrated in Figure 2A. *P. syringae* is divided into phylogroups, which broadly correspond to phylogenetic "species" sharing 95% Average Nucleotide Identity (ANI) (Gomila et al., 2017). The major plant pathogens belong to the "primary" phylogroups I, II, III, IV, V, VI and X, which form a monophyletic clade and rely on a canonical *hrp* type III secretion system (T3S) to cause disease. The "secondary" phylogroups VII, IX, XI and XIII include environment-associated strains which may not possess the *hrp* T3S and encode very few T3Es, consistent with their mostly non-pathogenic lifestyle (Dillon et al., 2019; Xin et al., 2018). To examine NADases across the species complex, an initial 2,437 genomes were obtained. After removing lower quality and almost identical genomes, 531 genomes were used in the final analysis. A phylogeny based on the core genome (Figure 2B) shows that these strains represent previously defined phylogroups and additional undefined clades. The genomes were grouped into ≥ 95% identical ANI groups which loosely correspond to defined phylogroups (Supplemental Figure S1). The primary phylogroups grouped at ≥ 85% ANI (highlighted in red on Figure 2B). The secondary phylogroups and other

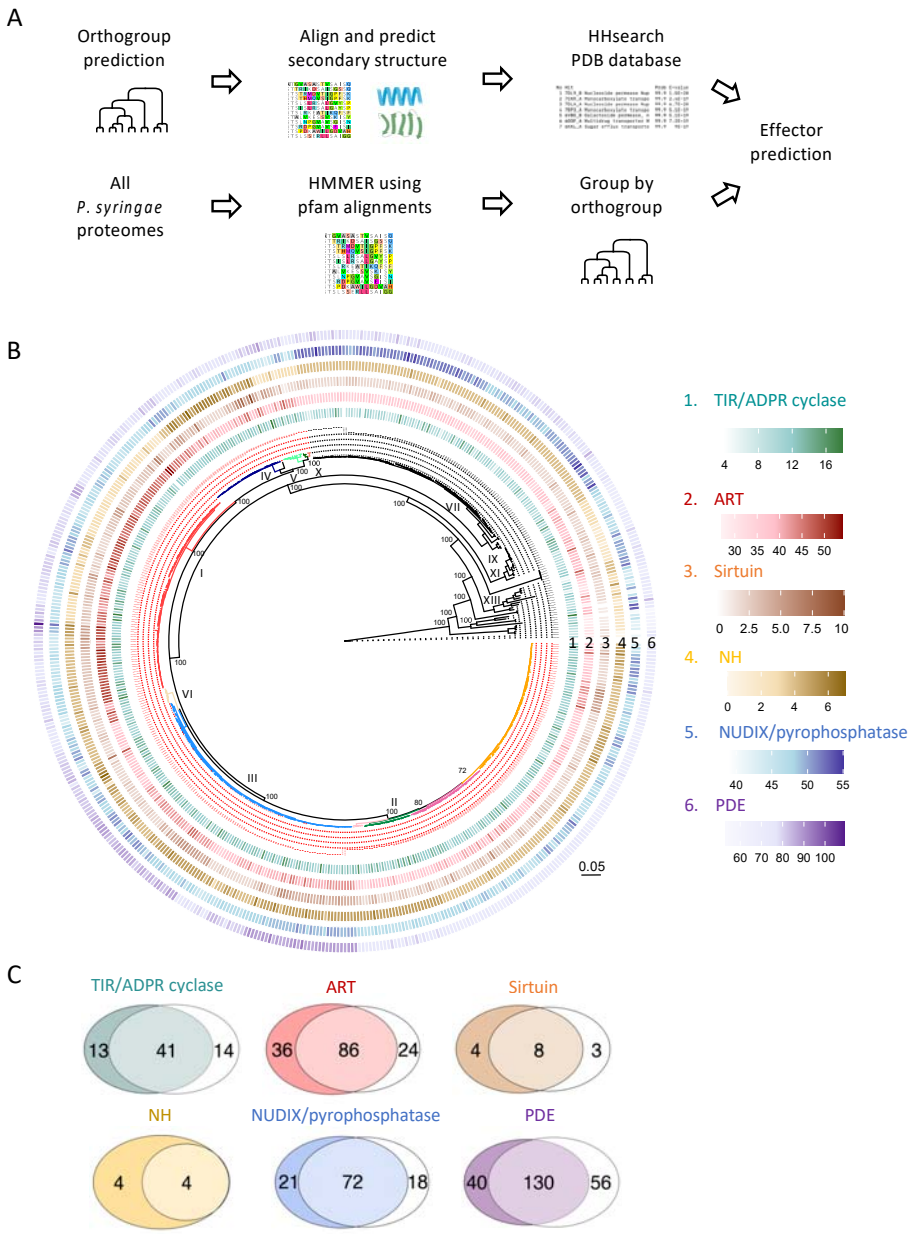

Figure 2. Identification of NADases encoded in the *P. syringae* species complex.

A) Two approaches based on HMMER and HHsearch respectively were used to predict all seven NAD hydrolyzing enzyme families from the pangenome of *P. syringae*.

B) NADase genes predicted across the *P. syringae* species complex are mapped onto the maximum-likelihood core genome phylogeny. Numbers of predicted genes from each enzyme family is presented by heatmaps. The phylogeny was generated based on 409 concatenated single copy core genes. The scale shows amino acid substitutions per site. Strains in the primary phylogroups are coloured in red. Due to similarity in enzymatic activity, NUDIX and pyrophosphatase were grouped together, as well as TIR and ADPR cyclase.

C) Venn diagrams to show the number of primary phylogroup specific NADase encoding orthogroups (left), orthogroups shared between primary and secondary phylogroups (middle), and orthogroups specific to secondary phylogroups (right).

genomes labelled as "*P. syringae*" were grouped outside the primary phylogroups at 80% ANI. Two divergent *P. viridiflava* strains, sharing 79% ANI with the rest of the

155 complex, were used as an out-group to root the tree. Orthology analysis defined the
156 pangenome of 2,867,287 protein-encoding genes into 23,583 orthogroups (OGs),
157 with an additional 11,608 singletons. In total, 35,191 OGs were further analyzed to
158 identify candidate NADases.
159
160 Two complementary approaches (HMMER and HHsearch) were employed to identify
161 proteins possessing any of the seven enzymatic domains including ART, NUDIX,
162 pyrophosphatase, PDE, TIR, sirtuin, ADPR cyclase, and nucleoside hydrolase
163 (Figure 2A; Supplemental Table S1). Using HMMER-based approach, 146 candidate
164 OGs were identified, whilst the HHsearch-based approach picked up 564
165 candidates, including 136 being identified by both approaches (Table 2, full details in
166 Supplemental Table S2). Among the 136 candidates are known housekeeping
167 nucleosidases, such as the NUDIX enzyme NudC (OG1452), the Sirtuin CobB3
168 (OG752), the purine nucleosidase RihA (OG2649), and cyclic-AMP
169 phosphodiesterase CpdA (OG3903) (Drabinska et al., 2020; Fuchs et al., 2010;
170 Gallego-Jara et al., 2021; Petersen and Moller, 2001). In addition, both searches
171 identified the TIR T3E HopAM1 (OG6638) (Eastman et al., 2022) and the ART T3E
172 HopU1 (OG9885) (Fu et al., 2007). The large number of hits (428) uniquely identified
173 from HHsearch indicates this method allowed the detection of divergent homologues.
174 By using both approaches, we maximized the chance of capturing all potential
175 candidates.
176
177 The 574 candidate OGs with potential NADase activity are distributed across the *P.*
178 *syringae* species complex (Figure 2B). On average, each *P. syringae* genome
179 contains 187 NADase-encoding genes, including 131 in core orthogroups (present in
180 ≥ 95% of genomes) and 56 in accessory orthogroups. The distribution of orthogroups
181 into core and accessory genomes varied for each enzyme group (Table 2). For
182 example, 34% of NUDIX/pyrophosphastase orthogroups are in the core genome,
183 whilst only 8% of TIR orthogroups are in the core genome. We next determined the
184 candidate NADase orthogroups specific to the primary phylogroups, which are
185 pathogens that rely on the *hrp* T3S for pathogenesis (Figure 2C; full data in
186 Supplemental Table S2). The majority of candidates are encoded in the genomes of
187 both groups, indicating that they are not directly related to pathogenesis. However, in

188 each enzyme family, there are orthogroups only encoded by the primary
189 phylogroups, suggesting that they may function as virulence factors or facilitate
190 pathogen adaptation to host environment.
191
192 **NADases as Type III effectors**
193
194 To identify T3Es from the NADase candidates, we established a pipeline, which
195 included an initial screen using the program EffectiveT3 (Eichinger et al., 2016)
196 followed by a promoter search for putative *hrp* boxes using FIMO (Grant et al.,
197 2011). Potential novel T3E candidates were further examined for the N-terminal
198 amino acid sequences for secretion signal characteristics (Guttman et al., 2002). The
199 outcome of this analysis revealed 13 OGs as high confidence effector candidates
200 (Table 3; Supplemental Figure S2; A full list before filtering is in Supplemental Table
201 S3). The robustness of this analysis is verified by the successful identification of all
202 the known T3Es with putative NADase-encoding domains: the ART effectors
203 HopF/HopBB, HopO1, AvrRpm, HopS, and HopU1, the NUDIX effector HopAG1, the
204 NH effector HopQ1, and the TIR effector HopAM1. The detection of multiple non-
205 overlapping hits to different enzymes in the same protein also revealed HopAG1 as a
206 multi-domain effector that contains an ART domain in addition to the previously
207 known NUDIX domain. Importantly, we identified five novel NADase T3E candidates,
208 including two ARTs (OG5256, OG18195), one PDE (OG4578), and two TIR/ADPR
209 cyclases (OG8567, OG18056).
210
211 The distribution of known NADase T3Es and novel candidates was mapped on the
212 core genome phylogeny (Figure 3A). 93% of the primary phylogroup strains have at
213 least one NADase T3Es and 72% possess T3Es belonging to more than one
214 enzyme family. On average, each primary phylogroup strain encodes three T3Es
215 that potentially hydrolyze NAD^+. Interestingly, three enzymatic activities that are each
216 represented by only one T3E are prevalent in primary phylogroup strains: the NUDIX
217 effector gene *hopAG1* is present in 55% of primary phylogroup strains across nine
218 phylogroups; the NH effector *hopQ1* is found in 31% of primary phylogroup strains
219 across five phylogroups; and the new PDE effector candidate OG4578 is found in
220 26% of primary phylogroup strains, although restricted to phylogroup II and X. These

results indicate NAD^+ hydrolysis is a key virulence strategy widely used by *P. syringae*.

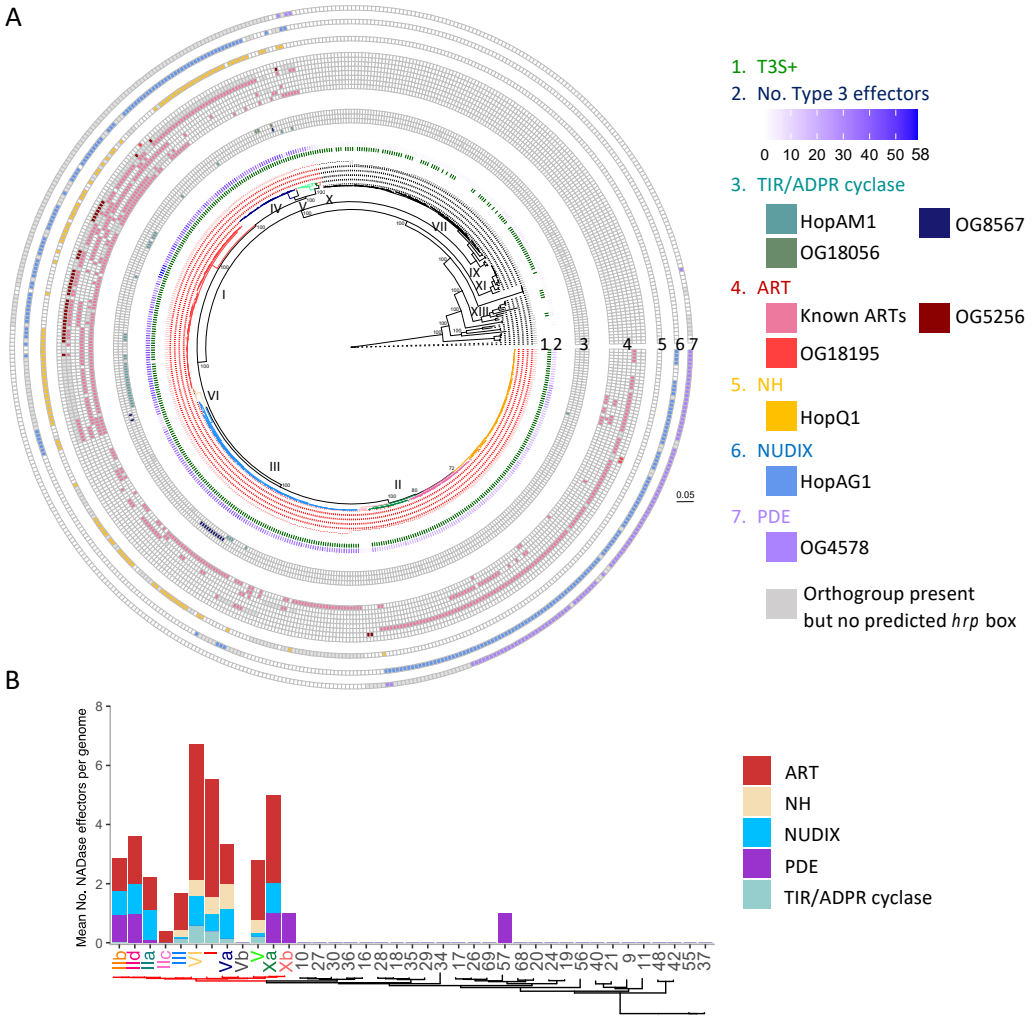

Figure 3. Predicted NADases as type III effectors in *P. syringae*.

A) NADase T3Es predicted across the *P. syringae* species complex are mapped onto the maximum-likelihood core genome phylogeny. Strains in the primary phylogroups are coloured in red. The presence of a canonical *hrp* T3SS is presented as Ring 1 (in green) and the number of known T3E genes encoded in each strain is presented in Ring 2 as a heatmap coloured in a scale of white to blue. Ring 3-7 each represents one of the five NADase enzyme families. Known T3Es with putative ART domains are in order: HopF/BB, HopO1, AvrRpm, HopS, HopU1, HopAG1. Presence of each orthogroup is coloured as in the scale, with grey squares indicating the orthogroup is present but with no *hrp* box in the promoter.

B) Mean number of NADase T3Es per phylogroup. The primary phylogroups are labelled with roman numerals, whilst secondary phylogroups correspond to their species number predicted by Average Nucleotide Identity in Supplemental Figure S1. A collapsed version of the core genome phylogeny, with the primary phylogroup clade in red is included for reference.

To better understand the diversity and distribution of NADase effectors in *P. syringae*, we summarize the average number of each enzyme group per genome in each phylogroup (Figure 3B; full details in Table 4). A clear difference between the

228 primary and secondary phylogroups can be visualized, with a significantly larger
229 number of NADase T3Es in the primary phylogroups. The number of ART effectors
230 per genome were particularly high in phylogroups I, VI, IVa, V and Xa. This could at
231 least in part be due to expansion of the HopO and HopF/HopBB families that has
232 been observed previously (Lo et al., 2017). A closer look at the copy number
233 variation of each ART effector across the phylogroups (Supplemental Figure S3)
234 shows that strains within phylogroups III, I and V possess up to four HopF/HopBB
235 family members, whilst HopO is specifically expanded in phylogroup I strains. An
236 increase in copy number was also noted for the TIR effector HopAM1 which is
237 present as two copies in 22% of the genomes that encode it. This observation
238 indicates the effectors may impact host processes in a dose-dependent manner.
239
240 In summary, this analysis demonstrate that the *P. syringae* species complex has
241 evolved effectors that contain diverse NADase domains, which potentially
242 manipulate levels of NAD^+ in the plant hosts. Many strains possess a variety of
243 enzyme groups with multiple gene copies, consistent with an important contribution
244 to virulence.
245
246 **Novel NADases T3E candidates**
247
248 ART is the largest NADase T3E family with eight members (six known and two
249 novel). Of the novel candidates, OG18195 is present in only three genomes in
250 phylogroups I and II, whilst OG5256 is present in 139 genomes. Structurally,
251 OG5256 is most similar to the T3E HopU1 (3U0J). Interestingly, *OG5256* gene was
252 found to be downstream of a T3E gene cluster harbouring *hopAG1*, *hopAH1* and
253 *hopAI1* (Supplemental Figure S2). The presence of these upstream effectors in a
254 putative operon may explain why only 37 of the 139 strains had a predicted *hrp* box
255 in the immediate upstream of this gene.
256
257 The candidate PDE effector OG4578 was identified as a protein with homology to
258 FimX EAL phosphodiesterase. FimX was reported to regulate twitching motility in
259 *Pseudomonas aeruginosa* (Kazmierczak et al., 2006), which is unlikely to be a T3E.
260 This OG was present in 238 primary phylogroup strains but only 100 had a predicted
261 *hrp* box promoter. These 100 strains are from a particular clade (Supplemental

262 Figure S4), indicating that OG4578 might be re-purposed to directly contribute to
263 pathogenesis.
264
265 Considering the recent breakthroughs in the functionality of TIR-NLR signalling, we
266 conducted in-depth analysis on the TIR/ADPR cyclase T3E candidates. HopAM1
267 was the only known TIR T3E from previous studies. Our analysis identified two
268 candidate T3Es: OG8567 as a TIR candidate and OG18056 as an ADPR cyclase
269 candidate. OG8567 is encoded in 22 strains including 15 in the primary phylogroups;
270 only genes in these 15 strains carry *hrp*-box-like promoter sequences. The second
271 candidate OG18056 was predicted as an ADPR cyclase. OG18056 is only present in
272 three *P. coronafaciens* pv. *atropurpurea* strains clustered in the primary phylogroup
273 IV which are pathogens of grass species. In the genome assembly
274 GCA_001400695, *OG18056* is within 15 Kb of T3E homologues *hopV1 and hopAA1*
275 and a coronatine biosynthesis operon (Supplemental Figures S2 and S5). In
276 addition, this gene is flanked by transposase genes and conjugation-machinery (*virB*
277 homologues), indicating that it is located in a mobile region of the genome and
278 therefore may have been acquired via horizontal gene transfer.
279
280 Using AlphaFold2 (Mirdita et al., 2022), we generated structure models for HopAM1,
281 OG8567, and OG18056 (Supplemental Figure S6A). The structures were aligned to
282 the TIR domain of the well-characterised human NADase SARM1, with Root-Mean-
283 Square Deviation (RMSD) values of 2.58, 2.78, and 3.01 Å, respectively
284 (Supplemental Figure S6B). A glutamate (Glu) in the position 642 aa in hSARM1 is
285 crucial for its NADase activity (Essuman et al., 2017). Structural alignments
286 confirmed that HopAM1 has a catalytic Glu (E191), as shown previously (Eastman et
287 al., 2022). Similarly, OG18056 also has a Glu (E305) at the corresponding position to
288 hSARM1-642, indicating that it could be an active NAD^+-cleaving enzyme. In
289 contrast, the other candidate OG8567 has an isoleucine (I142) at this position;
290 therefore it is less likely to possess NADase activity, or could have a suboptimally
291 positioned catalytic Glu in a nearby position (E139).
292
293 **OG18056 is a novel T3E with structural features similar to both TIR and ADPR**
294 **cyclase**
295

The full structural alignment of OG18056 with the hSARM1 TIR domain (Figure 4A) was intriguing because it was identified only from the HHsearch-based analysis, which revealed structural similarity only with ADPR cyclases. Superimposition of OG18056

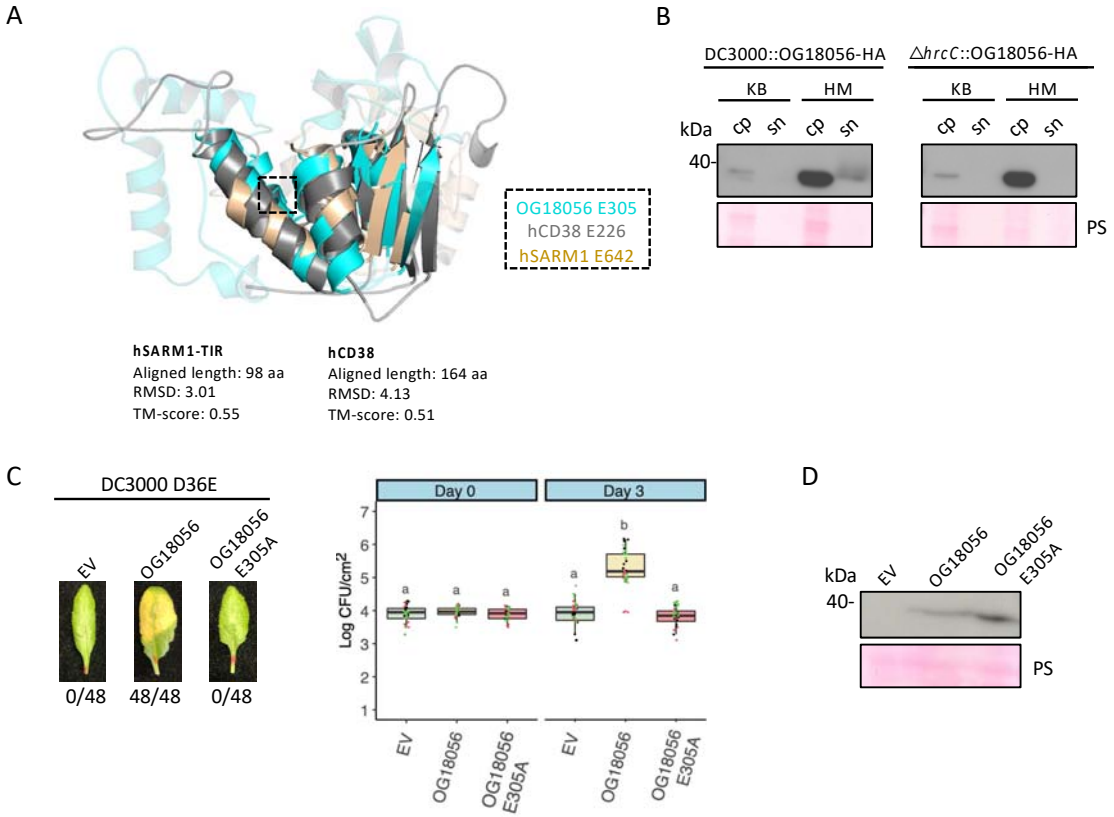

Figure 4. OG18056 is a novel T3E with similarity to ADPR cyclases.

A) Alignment of a structural model of OG18056 predicted by AlphaFold2 (in cyan) with human CD38 (6VUA, in grey) and the TIR domain of human SARM1 (6O0R, 561-700 aa, in light brown). Root-Mean-Square Deviation (RMSD) values and TM-scores are presented using OG18056 as the reference. For visualisation purposes, sequences outside the alignment region were removed and those that did not align within the region are more transparent. The predicted catalytic Glu residues are aligned in three structures and highlighted with a box.

B) Immunoblot showing the induction and secretion of OG18056 by *P. syringae*. OG18056-HA was expressed in PstDC3000 or the T3S mutant Δ*hrcC* under its native promoter. The bacteria were cultured in the rich medium Kings B (KB) or a Hrp-inducing minimal medium (HM). Proteins were extracted from cell pellet (cp) or supernatant (sn) and the protein levels of OG18056 were determined by western blotting using an anti-HA antibody. Ponceau S (PS) staining was used as the loading control.

C) OG18056 enhanced the virulence of the effectorless mutant PstDC3000 D36E on *Arabidopsis thaliana*. Upper: disease symptom development by D36E carrying the empty vector, OG18056 or OG18056(E305A). Numbers show the number of leaves with symptoms recorded over three independent experiments. Leaves were inoculated with 5 x 10^6 CFU/ml inoculum and imaged 3 days later. Lower: population count of the D36E transformants in *A. thaliana*. Boxplots show the day 0 and day 3 populations in Log CFU/cm^2. Individual data points with different colors represent results from three separate experiments. Tukey-HSD significance groups extracted from ANOVA are presented.

D) OG18056 and its mutant were expressed under its native promoter in PstDC3000 D36E. Immunoblot showing OG18056 and OG18056(E305A) expression when bacteria were grown in Hrp-inducing minimal medium.

with the human ADPR cyclase hCD38 showed a RMSD value of 4.13 Å. Although this RMSD value is higher (indicating lower similarity) than that of the hSARM1

303 alignment (3.01 Å), the alignment length was greater (164 aa) than that aligned to
304 hSARM1 (98 aa). In addition, OG18056-E305, which was aligned to the catalytic
305 residue (E642) in hSARM1, could also be aligned to the catalytic residue (E226) of
306 hCD38 (Munshi et al., 2000). Topology analysis indicated that the active sites of all
307 three enzymes have similar arrangement of alternating α helices and β sheets
308 (Supplemental Figure S7). These results suggest OG18056 is structurally similar to
309 both ADPR cyclase and TIR, hence may have a novel NADase activity.
310
311 To experimentally confirm that OG18056 is a T3E, we tested its expression pattern
312 and potential T3S-dependent secretion. The gene encoding OG18056 was
313 expressed in *P. syringae* strain PstDC3000 under its native promoter with a C-
314 terminal HA tag. The bacterial cells were induced in a *hrp*-minimal medium (HM);
315 total and secreted proteins were detected by immunoblotting (Figure 4B). Our results
316 showed that *OG18056* was drastically induced in the minimal medium, an
317 expression pattern commonly observed in T3S-related genes. Furthermore,
318 OG18056 proteins were detected in the supernatant of PstDC3000, but not a T3S
319 mutant Δ*hrcC*, confirming it is a true T3E that can be secreted in a T3S-dependent
320 manner.
321
322 To examine the potential virulence activity of OG18056 when delivered by bacteria
323 during infection, we expressed the gene in the effectorless mutant D36E of
324 PstDC3000. Inoculation of D36E expressing OG18056 (5 x 10^6 cfu/mL) into *A.*
325 *thaliana* leaves resulted in chlorotic symptoms (Figure 4C). *In planta* bacterial growth
326 (after inoculation at a lower dose, 5 x 10^5 cfu/mL) was also significantly increased.
327 Both virulence functions required the predicted catalytic residue E305, indicating that
328 the putative ADPR cyclase/TIR NADase activity is responsible for promoting
329 bacterial infection by this novel T3E. Both OG18056 and the E305A mutant were
330 confirmed to be expressed in D36E in *hrp*-inducing medium (Figure 4D).
331
332 **Characterization of NAD^+-binding residues in bacterial TIR proteins**
333
334 Different NADases produce specific products. The previously characterized TIR T3E
335 HopAM1 produces a variant of cADPR (3'-cADPR) that is different from the variant

2'-cADPR produced by plant TIRs (Manik et al., 2022). Over-expression of HopAM1 in *Nicotiana benthamiana* triggers cell death. This activity requires the catalytic residue E191, indicating that the cell death is induced either through the NADase products or NAD^+ depletion (Eastman et al., 2022). Interestingly, HopAM1 triggered cell death is independant of EDS1, indicating that it is through a pathway/mechanism distinctive from most plant TIR-NLRs (Choi et al., 2017). Residues in the catalytic pocket of NADases influence the preference of products after NAD^+ hydrolysis and can switch enzymatic activity between NAD^+ hydrolysis and cyclization (Graeff et al., 2009; Toshchakov and Neuwald, 2020). To gain insight into how this fine tuning of the NADase activity may affect the function of HopAM1, we investigated the structural diversity of the TIR and ADPR cyclase proteins in *P. syringae*.

Alphafold2 was used to generate 3D structure models for 63 of the 68 OGs predicted from *P. syringae* pangenome using the consensus sequence of each orthogroup (five were too short for structural prediction) (Figure 5A; Supplemental Table S4). 84% of the predictions scored ≥ 70 pLDDT (Predicted Local Distance Difference Test) indicating the prediction had worked well. We used the program P2RANK (Krivak and Hoksza, 2018) to predict if there was a ligand binding pocket in each protein and in parallel, alignments were performed with the TIR domain of hSARM1 to identify the positions of putative catalytic residues. The RMSD scores of the *P. syringae* proteins with hSARM1-TIR ranged from 1.75 to 5.47 Å, confirming structural homology (Supplemental Table S4). 43 proteins were predicted to have pockets at the position aligning to the hSARM1-TIR catalytic site. The structures of these 43 proteins were aligned pairwise using fr-tmalign (Pandit and Skolnick, 2008) and a dendrogram was constructed based on RMSD scores to represent their structural similarity (Figure 5B). The three T3E candidates were scattered across the dendrogram. OG18056 is clustered with other divergent TIR-like proteins outside the clade that showed higher similarity with hSARM1, consistent with our earlier analysis suggesting that OG18056 is more similar to ADPR cyclases.

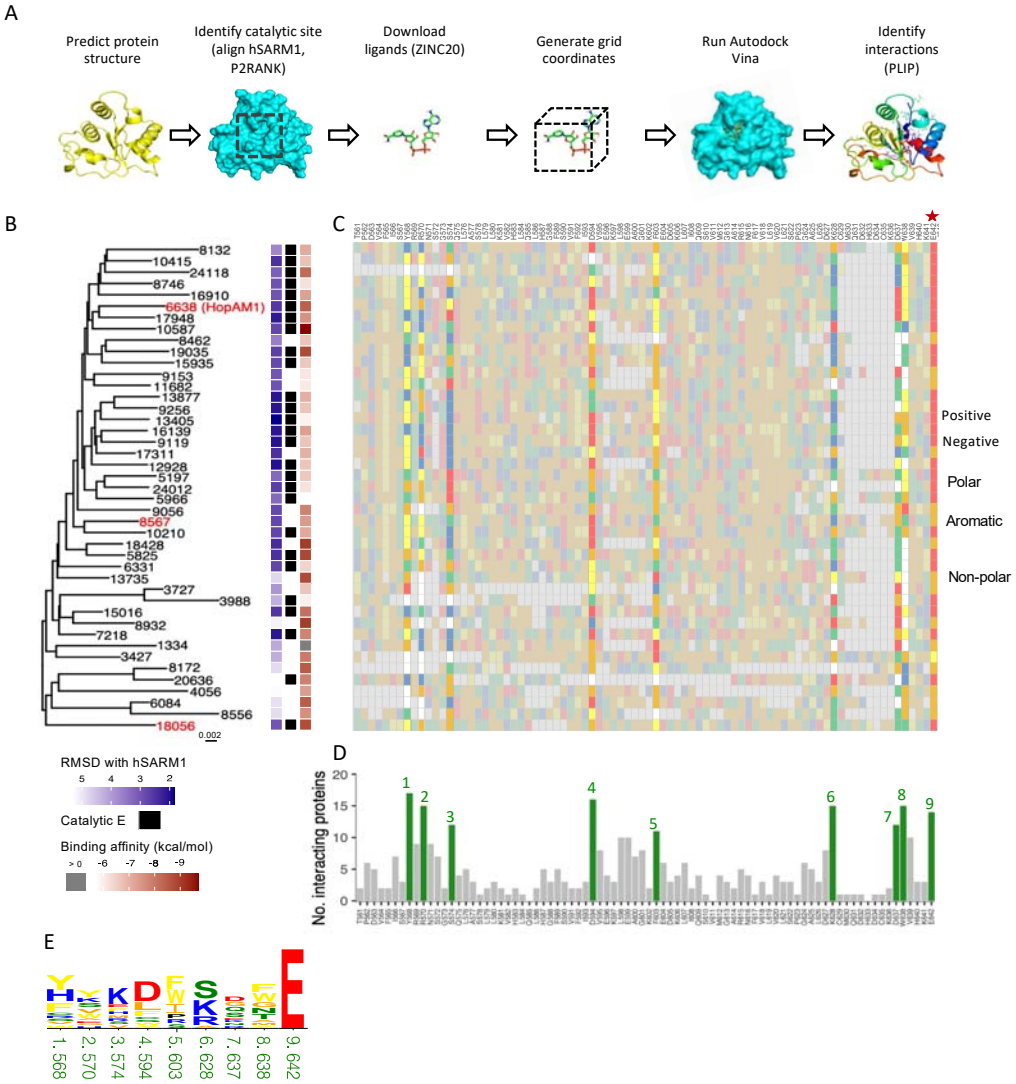

Figure 5. Structural analysis revealed diversity in the active site of *P. syringae* TIR proteins.

A) A bioinformatic pipeline used to generate 3D structure models of candidate NADases and predict NAD⁺-binding sites and residues.

B) A dendrogram based on structural similarity of 42 TIR proteins and the one ADPR cyclase homologue (OG18056) predicted from *P. syringae* pangenome. The dendrogram was built by the phylip program fitch using a distance matrix based on RMSD values from pairwise structural alignments. The RMSD values were normalized by alignment length. The three predicted TIR/ADPR cyclase T3Es are highlighted in red. Mapped onto the dendrogram is information regarding the structural alignment for each protein with hSARM1-TIR. The RMSD with hSARM1 is shown with a blue heatmap. A black box indicates that the protein had a glutamate aligning to the catalytic residue E642 in hSARM1-TIR. The NAD⁺ binding affinity of each protein is also presented.

C) Structually equivalent amino acids that aligned to hSARM1-TIR for each *P. syringae* TIR protein. The residues are ordered based on hSARM1-TIR positions and colour-coded by biochemical features. Nine positions that were frequently predicted to bind NAD⁺ during *in silico* docking are highlighted (also see D), whilst other positions are greyed out. The catalytic Glu (E642 in hSARM1-TIR) is labelled with a star.

D) Nine positions were predicted to bind NAD⁺ in more than ten *P. syringae* TIR proteins. These include residues corresponding the hSARM1 catalytic residue E642 (position 9), the nearby residues 628, 637 and 638 (positions 6-8), as well as residues 568, 570, 574, 594 and 603 (positions 1-5), which are further upstream.

E) Sequence logo generated for the nine positions that interacted with NAD⁺ showing frequency of different amino acids in each position. Amino acids are colour-coded as in (C).

We next conducted a docking analysis using Autodock Vina to model the binding of NAD⁺ within the pocket coordinates predicted by P2RANK (Figure 5A). From the

370 eight different models predicted from each structure, the NAD^+ binding affinity was
371 calculated using the top model from the prediction (Figure 5B). The results show
372 that most structures, except for one, bind NAD^+ with affinities ranging from -5.71 to -
373 9.72 kcal/mol (Supplemental Table S4). A monomeric hSARM1 TIR domain (561-
374 700 aa scored -7.20 kcal/mol, indicating the *P. syringae* TIRs had similar predicted
375 binding affinities to a known NADase). In summary, 42 of these proteins may have
376 the potential to bind NAD^+ through a TIR-like catalytic pocket and 27 of them have a
377 Glu aligned to the hSARM1-TIR catalytic residue E642, indicating that they may be
378 active NADases.
379
380 We next investigated whether there were particular positions that were important for
381 NAD^+ interaction. Using the structural alignment, we pulled out residues at each
382 structurally equivalent position to hSARM1-TIR from each *P. syringae* protein to
383 examine conservation (Figure 5C; Full region is presented in Supplemental Figure
384 S8). In parallel, the program plip (Salentin et al., 2015) was used to predict which
385 residues may interact with NAD^+ for each protein. Using hSARM1-TIR domain as a
386 reference, we then calculated the number of proteins that had a residue predicted to
387 interact with NAD^+ in each structurally equivalent position (Figure 5D). This analysis
388 revealed nine positions that were predicted to bind NAD^+ in more than ten proteins.
389 For clarity we refer to the positions based on the hSARM1 number. These include
390 residues corresponding the hSARM1 catalytic residue 642, as well as nearby
391 residues 628, 637 and 638. In addition, clusters of residues further upstream from
392 the catalytic Glu, corresponding to positions 568, 570, 574, 594 and 603 in hSARM1
393 were also frequently predicted to bind NAD^+. The higher frequency of the predicted
394 binding of these residues to NAD^+ may indicate their conserved importance in
395 substrate binding. Indeed, some of the equivalent positions have been shown to be
396 required for NAD^+-binding and/or NADase activity in ADPR cyclases (Liu et al.,
397 2007) and TIR proteins in plants and bacteria (Essuman et al., 2017; Horsefield et
398 al., 2020; Shi et al., 2022).
399
400 We also analyzed the conservation levels in each of the nine NAD^+-binding positions
401 across the *P. syringae* proteins (Supplemental Table S5). Except for the highly
402 conserved catalytic Glu residue (E642 in hSARM1-TIR), a high level of diversity was
403 observed in all other positions (Figure 5E). Nonetheless, some trends appear: 1)

404 aromatic residues (F, W or Y) were common at positions corresponding to hSARM1
405 568, 603 and 638; 2) positively charged residues (K or R) were common at positions
406 574 and 628; 3) position 594 was frequently negatively charged (D). Residues
407 corresponding to positions 568, 574, 594 and 638 were shown to modulate the
408 cyclase activity, substrate preference, and ratio of ADPR/cADPR products generated
409 by the CD38 homologues (Graeff et al., 2009; Ramakrishnan et al., 2010; Tohgo et
410 al., 1997). Therefore, specific residues in these positions may fine tune the
411 enzymatic activity.
412
413 **Functional analysis of the NAD^+-binding residues in HopAM1**
414
415 To experimentally examine the functional relevance of the nine NAD^+-binding
416 residues and their diversity, we generated mutants of HopAM1 that may alter its
417 activity. Because cADPRs have been shown to predominantly produced by plant
418 TIRs and HopAM1, we were interested in reducing the cyclase activity by changing
419 residues to those in hSARM1 and hCD38, which are greater NAD^+ hydrolases,
420 preferentially producing ADPR rather than cADPR. For this purpose, we generated
421 eight mutants with specific substitutions of six positions based on the corresponding
422 residues in either hSARM1 or hCD38. Some mutations were also made based on
423 studies of these positions in previous studies (Table 5). A previous study of hCD38
424 showed a negative amino acid at position corresponding to hSARM1 594 reduces
425 cyclase activity (Graeff et al., 2009). The residue in HopAM1 is D132 which is
426 already negatively charged, so we didn't generate any mutants of this residue. The
427 catalytic E191A mutant (position 642) was included as a control. The positions of
428 these residues in the HopAM1 structure docked with NAD^+ are presented in Figure
429 6A. These mutants were expressed in *N. benthamiana* using *Agro*-infiltration
430 (Supplemental Figure S9) and the cell death phenotype was monitored. The mutant
431 alleles were also expressed in the effectorless mutant D36E (introduced on the
432 plasmid pUCP20TK under the native *hopAM1* promoter) and infiltrated into *N.*
433 *benthamiana* leaves at a concentration of 2 x 10^8 cfu/mL in order to confirm the cell
434 death-triggering activities (Supplemental Figure S10). Similar observations were
435 made from both experiments.
436

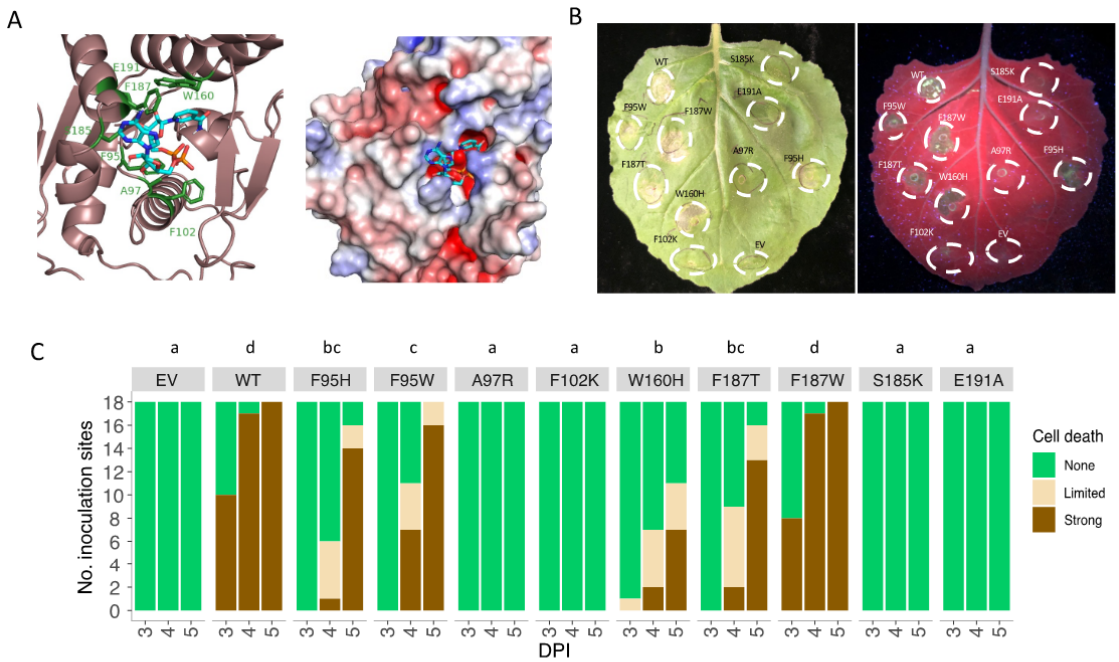

Figure 6. Characterization of NAD⁺-binding residues for cell death inducing activity of HopAM1.

A) Predicted structural model of HopAM1 docked with NAD⁺ with residues subjected to mutational analysis highlighted in green. The electrostatic image of the surface of HopAM1 active site is also presented with regions of positive, neutral and negative charge shown in blue, white and red respectively.

B) Cell death induced by HopAM1 and its mutants after transient expression in *N. benthamiana* by *Agro*-infiltration. Representative image of a *N. benthamiana* leaf five days post *Agro*-infiltration (DPI) is presented. The same leaf imaged under ultraviolet light is included to better visualize the cell death lesions. WT: wild-type; EV: empty vector.

C) Quantitative analysis of the cell death phenotype induced by various HopAM1 mutants. The appearance of cell death for each mutant was monitored at 3, 4, and 5 DPI, and scored as either no cell death (in green), weak cell death (limited, patchy appearance, in light brown) and strong cell death covering the whole inoculation site (dark brown). Statistical groupings of an ANOVA comparing cell death scores are shown above the graph. These results are from three independent experiments.

Three of the eight mutants, A97R, F102K, and S185K, showed no visible cell death, similar to the catalytic mutant E191A (Figure 6B; Figure 6C; Supplemental Figure S9). Both hCD38 and hSARM1, having a low cyclase activity, have an R at the corresponding position to A97 (see Table 5). Likewise, both hCD38 and hSARM1 have a K at the corresponding position to F102, and hSARM1 also has a K at the corresponding to S185. Therefore, these mutants could have reduced the cyclase activity of HopAM1, leading to no cell death.

Among the five mutants that were still able to cause cell death after 5 days, four showed slower and weaker phenotype. For residues F95 and F187, we made mutations to two different amino acids (F95 to W or H, and F187 to T or W).

450 Hydrophobic aromatic residues at these positions have been shown to alter the
451 activity and ADPR/cADPR product ratio of CD38 homologues (Graeff et al., 2009;
452 Ramakrishnan et al., 2010). Mutation of F95 to either W or H slowed down cell death
453 induction (Figure 6C). For F187, the F187T mutant exhibited weaker cell death,
454 whilst F187W was not significantly different from wild-type, indicating an aromatic
455 residue is important at this site. The cell death caused by the W160H mutant was
456 also weaker than the wild-type. Together, these results demonstrate that changes in
457 NADase activity altered the function of HopAM1 *in planta*.
458
459

460 **Discussion**

461

462 Recent research has brought the role of NAD^+-derived small molecules in host-
463 pathogen interactions into focus. It has become clear that the NADase activity
464 possessed by plant TIR proteins is essential for immune signaling (Bayless and
465 Nishimura, 2020). However, how pathogens may manipulate this key component of
466 immune system for the benefit of disease development is largely unknown.
467 Harnessing the pangenomic diversity and wealth of genetic resources of the model
468 bacterial pathogen *P. syringae*, we were able to conduct a near saturated search of
469 NADases and identified the NADase effector repertoire in this species complex.
470 Further structural analysis and experimental validation provide novel insight into the
471 functional diversity of NADase enzymes. Thus, this research advances our
472 understanding of NAD^+ manipulation as a important virulence strategy.

473

474 For NADase identification, we employed both a HMMER and HHsearch. Combining
475 both methods for domain identification was important because both approaches
476 have their own pros and cons. The HMMER approach searched all 2,867,287 *P.*
477 *syringae* protein sequences with high sensitivity and allowed specific searching of all
478 alleles within each of the > 35,000 orthogroups for similarity to a curated set of
479 sequences of defined domains. However, this analysis relied on what is already in
480 the pfam-seed alignment and may have missed remote homologues that do not
481 share significant sequence similarity (Pereira and Alva, 2021). For example,
482 the HopAG1 ART domain, OG5256, OG18195, OG4578, and OG18056 were not
483 identified by the HMMER search. The HHsearch approach used HMM-HMM
484 comparisons and added secondary structure information to identify hits in a
485 database. However, this approach relies on extracting hits annotated as the
486 enzymes of interest and thus depended on accurate annotation of database entries.
487 In addition, we only ran the consensus sequence of each orthogroup due to it being
488 computationally intensive, so could miss variation within orthogroups. Our results
489 clearly demonstrate the power of using a combination of methods for domain
490 identification. This pipeline could readily be applied to identify any protein or enzyme
491 families of interest. With the advent of rapid and accurate protein structural
492 prediction, integration of Alphafold2 structural models in functional annotation

pipelines such as this one will aid predictions where sequence-based approaches fail to pick up remote similarities in structure alone.

As a major metabolite and redox carrier, NAD^+ regulates various cellular processes. Consistently, we found a large amount of NADases encoded in each *P. syringae* genome, performing both house-keeping and accessory functions. Importantly, some NADases are specifically found in the primary phylogroups that are major plant pathogens, indicating that they may have specific roles in virulence or adaptation towards host environments. Although we focused on identifying T3Es in this study, it would be interesting to determine if any of these non-T3E NADases are *hrp*-regulated and thus may also contribute to pathogenesis. For example, Drabinska et al. (2020) identified multiple NUDIX enzymes in the animal opportunistic pathogen *P. aeruginosa* that are involved in virulence, production of the toxin pyocyanin, and resistance to oxidative stress.

Overall, *P. syringae* has a diverse set of T3Es with putative NADase activities. On average, primary phylogroup strains possess three NADase T3E genes per genome, with most possessing multiple T3Es with different enzymatic activities. Notably, we found a putative novel ART which may be in an operon with three other known T3Es. Within this operon the known effector HopAG1 also possesses both ART and NUDIX domains. We also identified a novel PDE candidate. It has been noted that host metabolism shifts drastically during PstDC3000 infection of *A. thaliana* (Drenichev et al., 2019; Ward et al., 2010). PstDC3000 possesses effectors with NADase activities, including two copies of the TIR effector HopAM1. These effectors may directly contribute to metabolomic changes seen in these previous studies. Previous studies on effector biology have been focused on protein targets in the host cells. Our results point to manipulation of host metabolites as a major virulence target.

Of the novel T3Es identified, OG18056 is predicted to have similarity to ADPR cyclases, which represents a novel virulence activity. Only eukaroytic ADPR cyclases such as CD38 have been characterized for their roles in physiology and immunity (Hogan et al., 2019). Previous studies have suggested there is limited sequence and structural similarity between TIRs and ADPR cyclases, however the pocket of OG18056 was able to align to both structures suggesting at least some

527 similarity in the folds that make up the catalytic pocket. It will be interesting to identify
528 the substrates and products of this effector and understand how they are related to
529 the virulence activity *in planta.* This effector is specifically found in pathogens of
530 grass species. The presence of nearby mobile elements indicates this effector is
531 likely within a plasmid/genomic island in these strains. A search of the protein
532 against NCBI using BLASTP showed homologues in *Pectobacteriaceae* including
533 plant-associated strains of *Pectobacterium* and *Brenneria* (Supplemental Table S6),
534 reinforcing the horizontal gene transfer hypothesis.
535
536 It has been shown that TIR domains like ADPR cyclases have multiple activities
537 including hydrolase, cyclase and base-exchange (Angeletti et al., 2022; Hogan et al.,
538 2019). Once NAD^+ is cleaved, the ADPR may transiently remain in the catalytic
539 pocket to be further modified for example via cyclisation or converted to other
540 products. The residues on the catalytic surface likely dictate the strength of binding,
541 orientation of ADPR and eventual products produced. Very recent structural
542 analyses have shown that various bacterial TIR proteins cyclise ADPR at differing
543 positions on the ribose sugar (Leavitt et al., 2022; Manik et al., 2022). Further
544 investigation of diverse TIRs across kingdoms may lead to the discovery of
545 additional small molecule variants with distinct roles. To add to this, the animal TIR
546 hSARM1 is known to have a range of activities which are regulated by the metabolic
547 state of the cell (Angeletti et al., 2022). How bacterial and plant TIR enzyme activities
548 are regulated remain to be explored.
549
550 We examined the diversity of *P. syringae* TIRs using AlphaFold2-based structural
551 modeling combined with NAD^+ docking. Our analysis identified 27 *P. syringae* TIRs
552 that could be activite NADase enzymes and detected a high degree of diversity at
553 the NAD^+-interacting residues, supporting that these enzymes could produce
554 different products involved in anti-viral defence, metabolic pathways and
555 pathogenesis. There are some caveats to this analysis: for example TIR domain
556 proteins often naturally form oligomers (Wan et al., 2019), so our monomeric
557 structural models may be missing information about pockets/active site interactions
558 that appear upon oligomerisation. In addition, purely *in silico* structural analysis may
559 miss biologically relevant conformational changes (Hofer et al., 2016). However, this
560 analysis can allow us to generate testable hypotheses. For example, conducting the

561 docking analysis across diverse structures allowed us to generate a list of potentially
562 important residues for functional analysis. Encouragingly, recent structural analysis
563 of plant and bacterial TIRs (Burdett et al., 2021; Manik et al., 2022) detected similar
564 positions that are involved in binding NAD^+ *in vitro*. Furthermore, specific
565 substitutions of these residues led to functional changes in HopAM1, confirming the
566 robustness of our analysis.
567
568 Several interesting observations were made through our HopAM1 mutagenesis
569 analysis: the F187T mutant was slower at inducing cell-death. This is consistent with
570 the recent finding that aromatic amino acids at positions corresponding to F187 in
571 other bacterial TIRs is specifically important for the cyclase activity (Manik et al.,
572 2022). Intriguingly, the mutant HopAM1(F187A) was not found to change cell death
573 induction in yeast (Eastman et al., 2021). Similarly, the F95 mutants (F95H and
574 F95W) and W160H triggered weaker cell death. Perhaps the enzymatic activity was
575 reduced due to the importance of these residues for substrate binding. An alternative
576 hypothesis is that the activity is altered and thus less of the 'cell-death' inducing
577 molecule is produced. Mutations F102K, S185K and A97R completely abolished cell
578 death. We were surprised that these mutations led to such drastic phenotypes as the
579 amino acids were changed to those in the corresponding positions in hSARM1 (for
580 S185 and A97) or hCD38 (for F102), and thereby should not abolish the enzymatic
581 activity. It would be interesting to see if the loss of cell-death observed for these
582 residues is due to a change in activity, such as the specific products produced. In
583 summary, our results support the idea that different TIR/ADPR cyclase active sites
584 vary and subtle differences in the amino acids across the sites modulate the
585 enzymatic reaction and the phenotypic consequences.
586
587 A key question is why would bacterial pathogens produce TIR effectors that may
588 trigger cell death? HopAM1 is known to trigger plant cell death in an EDS1-
589 independent manner (Choi et al., 2017), thus differing from most plant immune
590 receptor TNLs, which signal through EDS1 (Lapin et al., 2020). Phylogenomic
591 analysis has revealed some plant TIR proteins are also EDS1-independent
592 (Johanndrees et al., 2021). It is intriguing to speculate that variation in key active site
593 residues result in the differences in products of these TIR proteins, leading to distinct
594 phenotypes. How these effector produced molecules trigger cell death whilst

595 promoting virulence and if they can disrupt plant TIR signalling pathways through
596 molecular mimicry are important future questions. Our research paved the way of
597 conducting such investigation in the future.
598
599

Methods

Bacterial strains and plant material

Strains and plasmids used in this study are listed in Supplemental Table S7. *Pseudomonas* strains used in this study include *P. syringae* pv. tomato strain DC3000 (PstDC3000), the T3S mutant Δ*hrcC* (Yuan and He, 1996), and the effector-less mutant D36E (Wei et al., 2015). *P. coronafaciens* NCPPB 2397 (equivalent to ICMP 4457, genome assembly GCA_001400695) was used to clone the novel T3E OG18056. Antibiotics were used at the following concentrations kanamycin: 50 µg/mL, rifampicin: 50 µg/mL, carbenicillin: 100 µg/mL, gentamycin 50 µg/mL. These strains were used to inoculate *Nicotiana benthamiana* and *Arabidopsis thaliana* ecotype col-0 to examine cell death-triggering activities of HopAM1 and its mutants. *Agrobacterium tumerfaciens* strain GV3101 was used for *Agrobacterium*-mediated transient expression in *N. benthamiana*.

N. benthamiana plants were grown in a controlled growth room with 16:8 light:dark conditions at 22 °C, 80% humidity. *A. thaliana* plants were grown in a growth chamber with 10:14 light:dark conditions at 20 °C, 80% humidity. Five week old *N. benthamiana* and four week old *A. thaliana* were used for agro-infiltration and *P. syringae* inoculations.

Plasmid construction

Golden gate cloning (Engler et al., 2008) was used to generate constructs for transient expression of effectors in plants. Level 0 parts included: 35S long promoter, CDSNS (no stop) acceptor, 3xFLAG C-terminal tag, 35S terminator. The CDS were ordered from Twist Bioscience and PCR amplified using Phusion HR polymerase (ThermoFisher) to add golden gate compatible overhangs. Primers used in this study are presented in Supplemental Table S8. CDS were inserted into the level 0 CDSNS acceptor using one-pot digestion-ligation reaction with the restriction enzyme BpiI-HF (New England Biolabs). Level 0 fragments were then assembled into the *in planta* expression vector pICH47732.

632 Effector genes were also cloned into pUCP20TK for expression in *P. syringae*. For
633 *OG18056*, the genomic DNA containing CDS and its native promoter (250 bp
634 upstream of the start codon) was amplified from *P. coronafaciens* NCPPB 2397 with
635 the addition of a C-terminal HA tag in the reverse primer. For *hopAM1*, the wild-type
636 allele (encoded by PstDC3000) and nine mutants were synthesized with C-terminal
637 HA tags (Twist Bioscience) and PCR amplified to add overhangs for infusion cloning
638 (Takara). The *hopAM1* promoter sequence (207 bp upstream of the start codon) was
639 PCR amplified from PstDC3000 gDNA. Infusion cloning was used to insert promoter
640 and CDS fragments in reverse orientation to the *lacZ* promoter in the pUCP20TK
641 vector after linearisation of the vector with BamH1 and EcoR1 (New England
642 Biolabs). For generation of the E305A mutant of OG18056, a site-directed
643 mutagenesis approach using infusion was performed, splitting the gene and
644 promoter fragment into two PCR products for cloning with the mutation introduced in
645 primers R1 and F2. All constructs were confirmed by sanger sequencing. The
646 recombinant plasmids were electroporated into *P. syringae* as described in Choi et
647 al. (2006) apart from recovery growth was for 2 hours at 28 °C, 220 rpm.
648
649 **Agro-infiltration in *N. benthamiana***
650 *A. tumefaciens* GV3101 with various constructs was streaked from glycerol stocks
651 onto LBA plates containing appropriate antibiotics. Two-day old bacterial lawns were
652 resuspended in sterile distilled water and washed twice by spinning at 3000 rpm for
653 10 minutes. The cells were resuspended in $MgCl_2$-2-(N-morpholino)ethanesulfonic
654 acid (MES) buffer (10 mM $MgCl_2$, 10 mM MES, pH 5.6) to a final concentration of
655 OD_{600}=1.0 before adding acetosyringone to a final concentration of 150 µM. Bacteria
656 were incubated at room temperature (22 °C) for 3 hours before combining in a 1:1
657 ratio with the strain carrying the viral RNA silencing suppressor P19, meaning the
658 final OD_{600} of each *Agrobacterium* strain was 0.5. After *Agro*-infiltration, plants were
659 monitored for cell death symptoms for 3-5 days. Images were taken under natural
660 and UV light. Protein expression was confirmed by immunoblotting using total
661 proteins extracted from 1 cm leaf discs at 2 days post inoculation. Leaf discs were
662 immediately frozen in liquid nitrogen and stored at -80 °C. To extract proteins, 100
663 µL of protein extraction buffer (50 mM Tris-HCl (pH 7.5), 150 mM NaCl, 1 mM EDTA,
664 0.1% Triton X-100) was added and the discs were ground with a micropestle whilst

665 on ice. Crude plant material was removed by centrifugation at 11,000 x g for 15
666 minutes and 60 µL of the supernatant was combined with 30 µL 3X Laemmli buffer
667 (Laemmli, 1970) with 1x cOmplete EDTA-free protease inhibitor cocktail
668 (ThermoFisher) and boiled at 95°C for 5 minutes. Immunoblotting was performed as
669 described previously (Zhou et al., 2009). An anti-FLAG antibody conjugated to
670 horseradish peroxidase (Sigma) was used at 1:2000.
671
672 **Effector expression and secretion analysis**
673 To confirm that novel effector protein OG18056 was induced in Hrp-inducing minimal
674 medium and secreted in a T3S-dependent manner, PstDC3000 and the Δ*hrcC*
675 mutant carrying pUCP20TK::OG18056-HA were used for protein extraction. A
676 protocol based on (Vinatzer et al., 2005) was utilised to extract secreted proteins
677 from supernatents. The protocol was modified to extract from 8 mL of bacterial
678 supernatant (rather than 2 mL). Immunoblotting was performed as in Zhou et al.
679 (2009) using anti-HA from rat (Roche) at 1:1000, followed by a secondary anti-rat
680 antibody conjugated to horseradish peroxidase (sc-2750, Santa Cruz) at 1:2000. The
681 same protocol without supernatant extractions was used to confirm the expression of
682 OG18056 and HopAM1 in PstDC3000 D36E used in bacterial infection assays.
683
684 ***In planta Pseudomonas* assays**
685 PstDC3000 D36E carrying specific effector alleles or the pUCP20TK empty vector
686 were grown from glycerol stock for 2 days on agar plates at 28 °C, and the lawn was
687 resuspended in 10 mM $MgCl_2$ to the required optical density for inoculation. Cell
688 suspensions were syringe-infiltrated into *N. benthamiana* leaves at a concentration
689 of OD_{600} 0.4 (~2 x 10^8 cfu/mL). A lower concentration at 5 x 10^6 cfu/mL was used to
690 inoculate *A. thaliana*. Symptom development was recorded over several days and
691 pictures taken 3 days post inoculation. For bacterial population assays, inoculum
692 was prepared at 5 x 10^5 cfu/mL for *A. thaliana*. Bacteria were enumerated after 0
693 and 3 days by plating a dilution series on Kings B agar supplemented with rifampicin
694 and kanamycin.
695
696 **Genome retrieval and annotation**

697 2,437 *P. syringae* (taxid136849) genomes were download from NCBI on November
698 18th, 2020. Genomes were grouped into 806 clusters showing ≥ 99.95% ANI using
699 FastANI v1.32 (Jain et al., 2018). One genome per cluster was chosen based on the
700 assembly with the lowest number of contigs. Genomes were filtered using an
701 approach similar to Levy et al. (2018), removing those with ≥ 1000 contigs and an
702 N50 value lower than 40,000 bp computed with Quast (Gurevich et al., 2013).
703 Finally, CheckM (Parks et al., 2015) was used to select genomes with ≥ 95%
704 complete and < 5% contamination, leaving 531 genomes. Using a cut-off of ≥ 80%
705 ANI, all but two genomes are clustered into a single group. These two genomes
706 (GCA_ 900582625 and GCA_900573885) were kept as out-groups.

707 Genome annotation was performed using PROKKA (Seemann, 2014) and
708 Orthofinder (Emms and Kelly, 2019) was used to define orthogroups. To generate a
709 core genome phylogeny, 409 single copy orthogroups present in all genomes were
710 aligned using ClustalW (Thompson et al., 1994) with ends trimmed by Gblocks
711 (Castresana, 2000). Sequences were then concatenated into a 68,325 bp alignment,
712 converted to the phylip format and input into IQ-TREE2 (Minh et al., 2020) with
713 parameters JTT+I+G and 1000 bootstraps.

714 **Identification of Type III secretion system (T3S) and known Type III effectors**
715 **(T3Es)**

716 To identify genomes containing a canonical *hrp* T3S, a BLAST-based approach was
717 taken similar to that described in Dillon et al. (2019). T3S proteins from PstDC3000,
718 *P. syringae* pv. *syringae* B728A, and *P. viridiflava* LP23.1a (Supplemental Table S9
719 lists accession IDs) were used in a tBLASTn to query each genome. A genome was
720 determined to putatively encode a *hrp* T3S if it had a hit to every query with > 30%
721 length and > 30% identity for at least one of the three T3S inputs. A similar approach
722 was taken to determine which orthogroups corresponded to known T3E families in *P.*
723 *syringae*. A set of T3E protein sequences from pseudomonas-syringae.org was used
724 as input to query all orthogroups with BLASTp. Orthogroups containing proteins with
725 hit identities of 100% and E-value < $1x10^{-10}$ were determined to be those
726 corresponding to known T3Es.
727

728 **NADase T3E prediction**

729 The procedure employed to identify nucleosidase candidates in *P. syringae* is
730 presented in Figure 2A. HMMER (http://hmmer.org/) was used to search for proteins
731 carrying domains that are associated with different NADases. Pfam seed alignments
732 for enzyme families (listed in Supplemental Table S1) were obtained from Pfam
733 (http://pfam.xfam.org/) (downloaded on December 1st, 2020). The script hmmbuild
734 was used to create a HMM profile for each seed alignment. The command
735 hmmsearch was then used to screen all *P. syringae* proteins. HMMER results were
736 filtered based on a tolerant bit-score of ≥ 15 (Kloosterman et al., 2020) and grouped
737 by orthogroup. Orthogroups with positive hits were further filtered to remove those in
738 which less than 5% of the orthogroup members were a hit as these rare hits may not
739 represent the orthogroup function.
740
741 The program HHsearch (Soding et al., 2005) was also used for each orthogroup to
742 predict similarity to proteins in the PDB database (downloaded on October 28th,
743 2021). First, a multi-sequence alignment (MSA) was generated using ClustalW and a
744 consensus sequence for each orthogroup was generated using hhcon. Next, the
745 secondary structure of the consensus protein sequence was predicted by PSIPRED
746 and added to the alignment (Jones, 1999) before running HHsearch. Bash scripting
747 was used to extract candidates with hits towards NADase enzymes in the database
748 using a cutoff of ≥ 80% probability score. Two additional hits per protein with non-
749 overlapping regions were also identified, allowing proteins with multiple NADase
750 domains to be identified.
751
752 Candidate orthogroups predicted with HMMER or HHsearch were next screened
753 with EffectiveT3 (Eichinger et al., 2016) to determine if any could be T3Es.
754 Orthogroups containing hits with a score ≥ 0.9 were further analyzed for putative *hrp*
755 box sequences in their promoter region (within 1000 bp upstream of the protein-
756 coding sequence) using the program FIMO (Grant et al., 2011). The background
757 model was created using all promoters of all orthogroups and the *hrp* box sequence
758 GGAACC(15-17N)CCACNNA was used as the input. The program was run three
759 times to account for different size spacers.
760

761 Candidate T3Es were manually filtered based on the percentage of sequences within
762 the orthogroup predicted to be an effector (≥ 50%) and the percentage of these
763 sequences that contained a possible *hrp*-box promoter (≥ 25%). Orthogroups that
764 were only present in genomes without a predicted *hrp* T3S were removed.
765 Candidates T3Es were then manually examined to determine if they had
766 characteristic N-terminal characteristics associated with *P. syringae* T3Es (Guttman
767 et al., 2002; Petnicki-Ocwieja et al., 2002). The consensus sequence of each
768 orthogroup was examined for: 1) a high percentage of serines in the first 50 amino
769 acids; 2) an aliphatic amino acid in positions 3 or 4; and 3) a lack of negatively
770 charged residues within the first 12 positions. The genomic locations of each T3E
771 candidate gene were also manually examined using Geneious Prime 2022.0.1 to
772 examine gene neighbourhoods (https://www.geneious.com).
773
774 **Protein structure prediction and alignment**
775 Structural prediction was conducted using ColabFold AlphaFold2 batch with
776 MMseqs2 (Mirdita et al., 2022). The pipeline developed to identify the catalytic
777 pocket of each TIR protein and predict residues involved in NAD^+ binding is
778 illustrated in Figure 5A. For structural alignments, PDB files were aligned using fr-tm-
779 align (Pandit and Skolnick, 2008). Aligned residues, root-mean-square deviation
780 (RMSD) scores, and alignment lengths were extracted using bash scripting. To build
781 a dendrogram based on structural similarity, RMSD values from pairwise alignments
782 were extracted and standardised by dividing with alignment length. These values
783 were then converted to a distance matrix using R software. This distance matrix was
784 used as the input to the program fitch within phylip (v3.69) (Felsenstein, 2009). The
785 order of species was randomised in 100 independent runs.
786
787 Alignments were also conducted between each full-length *P. syringae* TIR protein
788 and the known NADase domain of the human TIR protein hSARM1 (structure
789 6O0R). Residues in the 561-700 aa fragment of hSARM1 were extracted with
790 PyMOL to create a PDB file of just the TIR domain to be used in the alignments. To
791 obtain the corresponding positions in CD38, alignments were also performed with
792 structures 6VUA and 1R12.
793

794 **Molecular docking of NAD^+**

795 Autodock Vina v1.2.3 (Eberhardt et al., 2021) was used for molecular docking.
796 P2Rank (Krivak and Hoksza, 2018) was first used to predict catalytic pocket sites.
797 Output files were processed with python to extract the pocket containing the catalytic
798 residues that aligned with hSARM1-TIR. Pocket coordinates were added to the Vina
799 config file for the docking run. The NAD^+ ligand was downloaded in 3D format from
800 https://zinc20.docking.org (Irwin et al., 2020) and converted to PDBQT format using
801 the Autodock Vina prepare_ligand script. The Radius of Gyration was calculated and
802 multiplied by 2.9 using python to generate the appropriate sized grid for ligand
803 binding (Feinstein and Brylinski, 2015). Autodock Vina was then ran with
804 exhaustiveness of 32 to produce eight possible models.

805

806 For each docked model, the protein and docked ligand PDBQT files were converted
807 back to PDB using open babel (O'Boyle et al., 2011) and concatenated to generate a
808 single file. This was then input into plip (v2.2.2) (Salentin et al., 2015) with default
809 parameters to predict bonds between NAD^+ and the protein. The plip output files of
810 all eight possible docked conformations were then combined to obtain all possible
811 protein residues that may bind to NAD^+ regardless of its orientation within the active
812 site.

813

814 **Figure creation**

815 PyMOL (https://pymol.org/2/) was used for visualisation of protein structures. The
816 Pro-origami online server was used for protein topology diagrams (Stivala et al.,
817 2011). WebLogo (http://weblogo.threeplusone.com/) was used to generate a
818 sequence logo of residues at particular positions in *P. syringae* TIR/ADPR cyclase
819 proteins. Biorender (BioRender.com) was used to create diagrams. All other figures
820 were created using R software (R.Core.Team, 2020). Specifically, the packages ape
821 (Paradis and Schliep, 2019), phangorn (Schliep, 2011), ggplot2 (Wickham, 2016),
822 ggtree (Guangchuang, 2020) and reshape (Wickham, 2007).

823

824 **Statistical analysis**

825 Analysis of variance (ANOVA) was used to statistically compare cell death
826 symptoms over time after *Agro*-infiltration as well as population counts of *P. syringae*
827 from *Arabidopsis*. Tukey-HSD significance groups were extracted using R packages

emmeans (Lenth, 2022) and the cld function within agricolae (de Mendiburu and Yaseen, 2020) .

Acknowledgments: We thank Dr. Alan Collmer for providing the *P. syringae* D36E mutant and Ma lab members for discussions and technical support. We thank Dan MacLean and George Deeks for bioinformatic analysis support. **Funding:** W.M. is supported by Gatsby Charitable Foundation and UKRI BBSRC Grant BBS/E/J/000PR9797. **Author Contributions:** W.M. and M.T.H. conceived the project. M.T.H. did the experiments and analyzed the data. W.M. and M.T.H. wrote the manuscript. **Competing Interests:** The authors declare no competing interests.

Data and material availability: All code are available at https://github.com/michhulin/ Pseudomonas. Materials are available from W.M. upon request under a materials transfer agreement with the Sainsbury Laboratory.

862 **Table 1. Characteristics of enzymes that can cleave NAD^+ including defining folds,**
863 **catalytic residues, known substrates and products.**

Group	Folds	Catalytic residues	Bond	Known role(s)	Activity	Substrates	Products	References
NUDIX	Nudix fold, beta-grasp domain, loop-helix-loop	RExxEE	Pyrophosphate/ phoshodiester	Hydrolase, removal of post-translational modifications	Hydrolysis	Pyro-phosphate bonds e.g. NADH	Various e.g. NMN, AMP	Srouji et al., (2017)
PDE	Phospho-esterase fold	H-H	Phosphodiester	Hydrolase	Hydrolysis	Various. cNMPs e.g. cAMP, DNA, RNA	various e.g. AMP	Turko et al. (1998), Akturk et al., (2018)
ART	ADP-ribosylating toxin turn-turn (ARTT) loop, phosphate-nicotinamide (PN) loop	ExE	N-glycosidic bond	Post-translation modification, DNA/RNA modification, NAD+ glycohydrolase	Hydrolysis, ribosyltransferase	NAD+	ADPR, NAM	Menetrey et al. (2008), Aravind et al. (2015)
SIR	Rossmann-fold domain	N, H	N-glycosidic bond	Post-translation modification	Hydrolysis, deacetylase, ribosyltransferase	NAD+	o-acetyl-ADPR, NAM	Sanders et al., (2010), Yuan and Marmorstein (2012)
TIR	Central parallel beta-sheet (βA-E) surrounded by alpha helices (αA–E)	E	N-glycosidic bond	Hydrolase	Hydrolysis, cyclase, base-exchange	NAD, NADP, NADH	ADPR, cADPR, v-cADPR, NAM, ADPRP, cADPRP, NAAD, NAADP, pRib-ADP, pRib-AMP, gcADPR, ADPR-ATP, diADPR	Ve et al. (2015),Essuman et al., (2017), Essuman et al., (2018), Angeletti et al., (2022), Huang et al. (2022), Leavitt et al. (2022), Jia et al. (2022)
ADPR cyclase	Central cleft between N and C-terminal domains forms active site	E	N-glycosidic bond	Hydrolase	Hydrolysis, cyclase, base-exchange	NAD, NADP, NADH, ADPR, Adenine	ADPR, cADPR, v-cADPR, NAADP, NAM, AP2A isomers, diADPR	Aarhus et al. (1995), Basile et al. (2005), Graeff et al., (2009), Grahnert et al. (2011)
NH	Central parallel beta-sheet surrounded by alpha helices	D-D	N-glycosidic bond	Hydrolase	Hydrolysis	Nucleosides, e.g. iP-riboside 5′-monophosphate	iP, PR	Garau et al. (2010), Li et al. (2013), Hann et al., (2014), Drenichev et al., (2018)

864
865
866

867 **Table 2. Numbers of putative NADase enzymes predicted by HHsearch and HMMER in**
868 **the *P. syringae* pangenome.**

	HHsearch	HHsearch unique	HMM	HMM unique	Shared	Complete	Core	Accessory
TIR/ ADPR cyclase	66	34	34	2	32	68	5	63
NUDIX/ Pyrophosphatase	109	81	30	2	28	111	38	73
ART	140	112	34	6	28	146	28	118
PDE	226	186	40	0	40	226	53	173
NH	8	3	5	0	5	8	2	6
SIR	15	12	3	0	3	15	2	13
Total	564	428	146	10	136	574	128	446

869

870

871 **Table 3. Predicted number of T3Es for each enzyme family in the *P. syringae***
872 **pangenome.**

Group	Total	EffectiveT3[a]	High frequency effectors[b]	T3SS+[c] and *hrp* promoter[d]	Manual filtering[e]
TIR/ADPR cyclase	68	36	14	7	3
NUDIX/ Pyrophosphatase	111	50	13	8	1
ART	146	74	26	14	7
PDE	226	114	43	20	1
NH	8	5	2	1	1
SIR	15	6	2	1	0
Total	574	285	100	51	13

873
874 a; Candidates with members scoring over 0.90 with EffectiveT3
875 b; Candidates where ≥ 50% of the orthogroup sequences were annotated as an effector
876 c; Candidates with effectors present in at least 1 genome with a canonical T3SS predicted
877 d; Candidates with ≥ 25% of the sequences possessed a proceeding *hrp*-box promoter
878 within 1000 bp (purposely set low in the case of possible operons)
879 e; Remaining candidates were manually checked, those within operons of non-effector
880 genes, or with a *hrp*-box promoter within other CDS or > 400bp away from the start codon
881 were removed
882
883

884 **Table 4. Known NADase T3Es and predicted candidates in *P. syringae.***

Group	Ortho-group	No. genes	No. effectors	% Effectors	No. *hrp* promoter	% *hrp* promoter	No. genomes	No. T3SS+ genomes	% T3SS+ genomes	Notes	Secretion signal score (out of 3)
ART	OG4303	339	332	98	299	90	188	187	99	HopF/BB	2
ART	OG5256	144	130	90	38	29	37	35	95	**Novel**	**3**
ART	OG5397	133	91	68	54	59	46	46	100	HopO1	3
ART	OG5686	112	103	92	91	88	87	87	100	AvrRpm	3
ART	OG6340	69	54	78	53	98	53	53	100	HopS	3
ART	OG9885	14	14	100	10	71	10	10	100	HopU1	3
ART	OG18195	3	3	100	3	100	3	3	100	**Novel**	**3**
ART[a]	OG4463	297	223	75	213	96	213	213	100	HopAG1	3
NH	OG4871	195	124	64	121	98	118	117	99	HopQ1	2
NUDIX	OG4463	297	223	75	213	96	213	213	100	HopAG1	3
PDE	OG4578	258	214	83	102	48	101	100	99	**Novel**	**2**
TIR	OG6638	55	49	89	45	92	38	37	97	HopAM1	3
TIR	OG8567	23	21	91	15	71	14	14	100	**Novel**	**2**
TIR	OG18056	3	3	100	3	100	3	3	100	**Novel**	**3**

885
886 No. genes: number of genes in orthogroup.
887 No. effectors: number of genes within orthogroup that were predicted to encode an effector.
888 % effectors: % orthogroup that may code effector.
889 No. *hrp* promoter: Number of predicted effector genes per orthogroup that had a predicted *hrp* box
890 % *hrp* promoter: % effector genes in orthogroup that had *hrp* promoter.
891 No. T3S+ genomes: Number of genomes encoding the genes in each orthogroup predicted as
892 effectors with a *hrp* box which have the genes required for T3S machinery.
893 % genomes with T3S+: % of effector genes with a *hrp* box per orthogroup that were in T3S+
894 genomes.
895 Secretion signal score: A score from 0-3 based on three previously defined criteria of T3E secretion
896 signals:1) a high % serines; 2) a lack of negative amino acids in the first 12 residues; 3) an aliphatic
897 amino acid at position 3 or 4.
898 [a]Although the main hit of OG0004463 (HopAG1) was a NUDIX domain, a further domain with
899 homology to ART was predicted at a different region of the protein.
900
901

902 **Table 5. Information on the nine putative interacting sites across the catalytic sites of**
903 **TIR/ADPR cyclases with rationale behind mutational strategy.**

No. *P.s* TIRs interacting	HopAM1 (C?)	SARM1 (Ac)	OG 18056 (?)	hCD38 (Ac)	aCD38 (aC)	Mutants	Outcome	Reasoning	Notes
17	F95*	Y568	W149	W125	W77	H, W	Slower cell death	Change to similar residue to modify activity	Ramakrishnan et al., (2010) changed corresponding residue in SpARC4 cyclase (CD38 homologue) from Y to either W or H and reduced cyclase activity
15	A97	R570	G151	R127	G79	R	No cell death	Change to SARM1/CD38 residue to alter activity	Liu et al., (2009) showed this residue R127 is involved in CD38 binding NAD+
12	F102	S574	M164	K129	Y81	K	No cell death	Changed to K based on CD38 lack of cyclase and aCD38 having similar hydrophobic residue	Tohgo et al., (1997) reported K129 in CD38 important for cADPR hydrolysis rather than hydrolysis of NAD+. K129 may also be target of ADP-ribosylation to modify the active site Jiang et al. (2013)
11	W160	F603	W263	W189	W140	H	Slower cell death	Change to non-hydrophobic related amino acid to alter binding	W at this position in CD38 is generally important for binding NAD+ (Liu et al. (2009),Wolters et al. (2019)
15	S185	K628	N291	N217	R170	K	No cell death	Change to SARM1 residue K to see if alters activity	Summers et al. (2016) showed K628 in SARM1 is important for activity.
15	F187*	W638	T300	T221	F174	T, W	Slower cell death in T mutant	Change to similar residues as in CD38 papers	Graeff et al., (2009) found mutation from F to T reduced cyclase activity of the cyclase aCD38 without drastically changing hydrolase
14	E191	E642	E305	E226	E179	A	None	Act as a control to show mutation expected	Identified catalytic site of TIRs (Essuman et al. (2017); Horsefield et al. (2019; Eastman et al. (2021)

904
905 A: produces ADPR, C: produces cyclic-ADPR. Lower case is where the activity of lower than the other
906 activity (in uppercase). ? means products are unknown. * For two well studied residues in CD38 these
907 residues in HopAM1 were changed to two different amino acids based on previous work of specifically
908 altering activity.
909

910 **Figure legends**

911

912 **Figure 1. Enzyme families that may hydrolyse NAD^+.**

913 The NUDIX (nucleoside diphosphate linked to a variable moiety X) enzymes and
914 phosphodiesterases (PDEs) cleave the pyrophosphate bond. ADP-
915 ribosyltransferases (ART), nucleoside hydrolases (NH), ADPR cyclases, and sirtuins
916 cleave the N-glycosidic bond.

917

918 **Figure 2. Identification of NADases encoded in the *P. syringae* species**
919 **complex.**

920 A) Two approaches based on HMMER and HHsearch respectively were used to
921 predict all seven NAD hydrolyzing enzyme families from the pangenome of *P.*
922 *syringae*.

923 B) NADase genes predicted across the *P. syringae* species complex are mapped
924 onto the maximum-likelihood core genome phylogeny. Numbers of predicted
925 genes from each enzyme family is presented by heatmaps. The phylogeny was
926 generated based on 409 concatenated single copy core genes. The scale shows
927 amino acid substitutions per site. Strains in the primary phylogroups are coloured
928 in red. Due to similarity in enzymatic activity, NUDIX and pyrophosphatase were
929 grouped together, as well as TIR and ADPR cyclase.

930 C) Venn diagrams to show the number of primary phylogroup specific NADase
931 encoding orthogroups (left), orthogroups shared between primary and secondary
932 phylogroups (middle), and orthogroups specific to secondary phylogroups (right).

933

934 **Figure 3. Predicted NADases as type III effectors in *P. syringae*.**

935 A) NADase T3Es predicted across the *P. syringae* species complex are mapped onto
936 the maximum-likelihood core genome phylogeny. Strains in the primary
937 phylogroups are coloured in red. The presence of a canonical *hrp* T3SS is
938 presented as Ring 1 (in green) and the number of known T3E genes encoded in
939 each strain is presented in Ring 2 as a heatmap coloured in a scale of white to
940 blue. Ring 3-7 each represents one of the five NADase enzyme families. Known
941 T3Es with putative ART domains are in order: HopF/BB, HopO1, AvrRpm, HopS,
942 HopU1, HopAG1. Presence of each orthogroup is coloured as in the scale, with

943 grey squares indicating the orthogroup is present but with no *hrp* box in the
944 promoter.
945 B) Mean number of NADase T3Es per phylogroup. The primary phylogroups are
946 labelled with roman numerals, whilst secondary phylogroups correspond to their
947 species number predicted by Average Nucleotide Identity in Supplemental Figure
948 S1. A collapsed version of the core genome phylogeny, with the primary
949 phylogroup clade in red is included for reference.
950
951 **Figure 4. OG18056 is a novel T3E with similarity to ADPR cyclases.**
952 A) Alignment of a structural model of OG18056 predicted by AlphaFold2 (in cyan)
953 with human CD38 (6VUA, in grey) and the TIR domain of human SARM1 (6O0R,
954 561-700 aa, in light brown). Root-Mean-Square Deviation (RMSD) values and TM-
955 scores are presented using OG18056 as the reference. For visualisation
956 purposes, sequences outside the alignment region were removed and those that
957 did not align within the region are more transparent. The predicted catalytic Glu
958 residues are aligned in three structures and highlighted with a box.
959 B) Immunoblot showing the induction and secretion of OG18056 by *P. syringae*.
960 OG18056-HA was expressed in PstDC3000 or the T3S mutant Δ*hrcC* under its
961 native promoter. The bacteria were cultured in the rich medium Kings B (KB) or a
962 Hrp-inducing minimal medium (HM). Proteins were extracted from cell pellet (cp)
963 or supernatant (sn) and the protein levels of OG18056 were determined by
964 western blotting using an anti-HA antibody. Ponceau S (PS) staining was used as
965 the loading control.
966 C) OG18056 enhanced the virulence of the effectorless mutant PstDC3000 D36E on
967 *Arabidopsis thaliana*. Upper: disease symptom development by D36E carrying the
968 empty vector, OG18056 or OG18056(E305A). Numbers show the number of
969 leaves with symptoms recorded over three independent experiments. Leaves
970 were inoculated with 5 x 10^6 CFU/ml inoculum and imaged 3 days later. Lower:
971 population count of the D36E transformants in *A. thaliana*. Boxplots show the day
972 0 and day 3 populations in Log CFU/cm^2. Individual data points with different
973 colors represent results from three separate experiments. Tukey-HSD significance
974 groups extracted from ANOVA are presented.

975 D) OG18056 and its mutant were expressed under its native promoter in PstDC3000
976 D36E. Immunoblot showing OG18056 and OG18056(E305A) expression when
977 bacteria were grown in Hrp-inducing minimal medium.

978 **Figure 5. Structural analysis revealed diversity in the active site of *P. syringae***
979 **TIR proteins.**

980 A) A bioinformatic pipeline used to generate 3D structure models of candidate
981 NADases and predict NAD^+-binding sites and residues.
982 B) A dendrogram based on structural similarity of 42 TIR proteins and the one ADPR
983 cyclase homologue (OG18056) predicted from *P. syringae* pangenome. The
984 dendrogram was built by the phylip program fitch using a distance matrix based
985 on RMSD values from pairwise structural alignments. The RMSD values were
986 normalized by alignment length. The three predicted TIR/ADPR cyclase T3Es are
987 highlighted in red. Mapped onto the dendrogram is information regarding the
988 structural alignment for each protein with hSARM1-TIR. The RMSD with hSARM1
989 is shown with a blue heatmap. A black box indicates that the protein had a
990 glutamate aligning to the catalytic residue E642 in hSARM1-TIR. The NAD^+
991 binding affinity of each protein is also presented.
992 C) Structually equivalent amino acids that aligned to hSARM1-TIR for each *P.*
993 *syringae* TIR protein. The residues are ordered based on hSARM1-TIR positions
994 and colour-coded by biochemical features. Nine positions that were frequently
995 predicted to bind NAD^+ during *in silico* docking are highlighted (also see D), whilst
996 other positions are greyed out. The catalytic Glu (E642 in hSARM1-TIR) is
997 labelled with a star.
998 D) Nine positions were predicted to bind NAD^+ in more than ten *P. syringae* TIR
999 proteins. These include residues corresponding the hSARM1 catalytic residue
1000 E642 (position 9), the nearby residues 628, 637 and 638 (positions 6-8), as well
1001 as residues 568, 570, 574, 594 and 603 (positions 1-5), which are further
1002 upstream.
1003 E) Sequence logo generated for the nine positions that interacted with NAD^+ showing
1004 frequency of different amino acids in each position. Amino acids are colour-coded
1005 as in (C).
1006

1007 **Figure 6. Characterization of NAD^+-binding residues for cell death inducing**
1008 **activity of HopAM1.**

1009 A) Predicted structural model of HopAM1 docked with NAD^+ with residues subjected
1010 to mutational analysis highlighted in green. The electrostatic image of the surface
1011 of HopAM1 active site is also presented with regions of positive, neutral and
1012 negative charge shown in blue, white and red respectively.
1013 B) Cell death induced by HopAM1 and its mutants after transient expression in *N.*
1014 *benthamiana* by Agro-infiltration. Representative image of a *N. benthamiana* leaf
1015 five days post Agro-infiltration (DPI) is presented. The same leaf imaged under
1016 ultraviolet light is included to better visualize the cell death lesions. WT: wild-type;
1017 EV: empty vector.
1018 C) Quantitative analysis of the cell death phenotype induced by various HopAM1
1019 mutants. The appearance of cell death for each mutant was monitored at 3, 4, and
1020 5 DPI, and scored as either no cell death (in green), weak cell death (limited,
1021 patchy appearance, in light brown) and strong cell death covering the whole
1022 inoculation site (dark brown). Statistical groupings of an ANOVA comparing cell
1023 death scores are shown above the graph. These results are from three
1024 independent experiments.
1025
1026

Parsed Citations

Aarhus, R., Graeff, R.M., Dickey, D.M., Walseth, T.F., and Lee, H.C. (1995). ADP-ribosyl cyclase and CD38 catalyze the synthesis of a calcium-mobilizing metabolite from NADP. J Biol Chem 270, 30327-30333.
Google Scholar: Author Only Title Only Author and Title

Adlung, N., Prochaska, H., Thieme, S., Banik, A., Bluher, D., John, P., Nagel, O., Schulze, S., Gantner, J., Delker, C., et al. (2016). Non-host Resistance Induced by the Xanthomonas Effector XopQ Is Widespread within the Genus Nicotiana and Functionally Depends on EDS1. Front Plant Sci 7, 1796.
Google Scholar: Author Only Title Only Author and Title

Akturk, A., Wasilko, D.J., Wu, X., Liu, Y., Zhang, Y., Qiu, J., Luo, Z.Q., Reiter, K.H., Brzovic, P.S., Klevit, R.E., et al. (2018). Mechanism of phosphoribosyl-ubiquitination mediated by a single Legionella effector. Nature 557, 729-733.
Google Scholar: Author Only Title Only Author and Title

Angeletti, C., Amici, A., Gilley, J., Loreto, A., Trapanotto, A.G., Antoniou, C., Merlini, E., Coleman, M.P., and Orsomando, G. (2022). SARM1 is a multi-functional NAD(P)ase with prominent base exchange activity, all regulated bymultiple physiologically relevant NAD metabolites. iScience 25, 103812.
Google Scholar: Author Only Title Only Author and Title

Aravind, L., Zhang, D., de Souza, R.F., Anand, S., and Iyer, L.M. (2015). The natural history of ADP-ribosyltransferases and the ADP-ribosylation system. Curr Top Microbiol Immunol 384, 3-32.
Google Scholar: Author Only Title Only Author and Title

Azevedo, M.F., Faucz, F.R., Bimpaki, E., Horvath, A., Levy, I., de Alexandre, R.B., Ahmad, F., Manganiello, V., and Stratakis, C.A. (2014). Clinical and molecular genetics of the phosphodiesterases (PDEs). Endocr Rev 35, 195-233.
Google Scholar: Author Only Title Only Author and Title

Basile, G., Taglialatela-Scafati, O., Damonte, G., Armirotti, A., Bruzzone, S., Guida, L., Franco, L., Usai, C., Fattorusso, E., De Flora, A., et al. (2005). ADP-ribosyl cyclases generate two unusual adenine homodinucleotides with cytotoxic activity on mammalian cells. Proc Natl Acad Sci U S A 102, 14509-14514.
Google Scholar: Author Only Title Only Author and Title

Bayless, A.M., and Nishimura, M.T. (2020). Enzymatic Functions for Toll/Interleukin-1 Receptor Domain Proteins in the Plant Immune System. Front Genet 11, 539.
Google Scholar: Author Only Title Only Author and Title

Burdett, H., Hu, X., Rank, M.X., Maruta, N., and Kobe, B. (2021). Self-association configures the NAD+-binding site of plant NLR TIR domains. BioRxiv.
Google Scholar: Author Only Title Only Author and Title

Castresana, J. (2000). Selection of Conserved Blocks from Multiple Alignments for Their Use in Phylogenetic Analysis. Mol Biol Evol 17, 540–552.
Google Scholar: Author Only Title Only Author and Title

Choi, K.H., Kumar, A., and Schweizer, H.P. (2006). A 10-min method for preparation of highly electrocompetent Pseudomonas aeruginosa cells: application for DNA fragment transfer between chromosomes and plasmid transformation. J Microbiol Methods 64, 391-397.
Google Scholar: Author Only Title Only Author and Title

Choi, S., Jayaraman, J., Segonzac, C., Park, H.J., Park, H., Han, S.W., and Sohn, K.H. (2017). Pseudomonas syringae pv. actinidiae Type III Effectors Localized at Multiple Cellular Compartments Activate or Suppress Innate Immune Responses in Nicotiana benthamiana. Front Plant Sci 8, 2157.
Google Scholar: Author Only Title Only Author and Title

Corda, D., and Di Girolamo, M. (2003). Functional aspects of protein mono-ADP-ribosylation. The EMBO Journal 22, 1953–1958.
Google Scholar: Author Only Title Only Author and Title

Coronas-Serna, J.M., Louche, A., Rodriguez-Escudero, M., Roussin, M., Imbert, P.R.C., Rodriguez-Escudero, I., Terradot, L., Molina, M., Gorvel, J.P., Cid, V.J., et al. (2020). The TIR-domain containing effectors BtpA and BtpB from Brucella abortus impact NAD metabolism. PLoS Pathog 16, e1007979.
Google Scholar: Author Only Title Only Author and Title

de Mendiburu, F., and Yaseen, M. (2020). agricolae: Statistical Procedures for Agricultural Research.R package version 1.4.0.

Dillon, M.M., Thakur, S., Almeida, R.N.D., Wang, P.W., Weir, B.S., and Guttman, D.S. (2019). Recombination of ecologically and evolutionarily significant loci maintains genetic cohesion in the Pseudomonas syringae species complex. Genome Biol 20, 3.
Google Scholar: Author Only Title Only Author and Title

Dong, S., Yin, W., Kong, G., Yang, X., Qutob, D., Chen, Q., Kale, S.D., Sui, Y., Zhang, Z., Dou, D., et al. (2011). Phytophthora sojae

avirulence effector Avr3b is a secreted NADH and ADP-ribose pyrophosphorylase that modulates plant immunity. PLoS Pathog 7, e1002353.
Google Scholar: Author Only Title Only Author and Title

Drabinska, J., Ziecina, M., Modzelan, M., Jagura-Burdzy, G., and Kraszewska, E. (2020). Individual Nudix hydrolases affect diverse features of Pseudomonas aeruginosa. MicrobiologyOpen 9, e1052.
Google Scholar: Author Only Title Only Author and Title

Drenichev, M.S., Bennett, M., Novikov, R.A., Mansfield, J., Smirnoff, N., Grant, M., and Mikhailov, S.N. (2019). A role for 3'-O-beta-D-ribofuranosyladenosine in altering plant immunity. Phytochemistry 157, 128-134.
Google Scholar: Author Only Title Only Author and Title

Duxbury, Z., Wang, S., MacKenzie, C.I., Tenthorey, J.L., Zhang, X., Huh, S.U., Hu, L., Hill, L., Ngou, P.M., Ding, P., et al. (2020). Induced proximity of a TIR signaling domain on a plant-mammalian NLR chimera activates defense in plants. Proc Natl Acad Sci U S A 117, 18832-18839.
Google Scholar: Author Only Title Only Author and Title

Eastman, S., Smith, T., Zaydman, M.A., Kim, P., Martinez, S., Damaraju, N., DiAntonio, A., Milbrandt, J., Clemente, T.E., Alfano, J.R., et al. (2022). A phytobacterial TIR domain effector manipulates NAD(+) to promote virulence. New Phytol 233, 890-904.
Google Scholar: Author Only Title Only Author and Title

Eberhardt, J., Santos-Martins, D., Tillack, A.F., and Forli, S. (2021). AutoDock Vina 1.2.0: New Docking Methods, Expanded Force Field, and Python Bindings. J Chem Inf Model 61, 3891-3898.
Google Scholar: Author Only Title Only Author and Title

Eichinger, V., Nussbaumer, T., Platzer, A., Jehl, M.A., Arnold, R., and Rattei, T. (2016). EffectiveDB--updates and novel features for a better annotation of bacterial secreted proteins and Type III, IV, VI secretion systems. Nucleic Acids Res 44, D669-674.
Google Scholar: Author Only Title Only Author and Title

Emms, D.M., and Kelly, S. (2019). OrthoFinder: phylogenetic orthology inference for comparative genomics. Genome Biol 20, 238.
Google Scholar: Author Only Title Only Author and Title

Engler, C., Kandzia, R., and Marillonnet, S. (2008). A one pot, one step, precision cloning method with high throughput capability. PLoS One 3, e3647.
Google Scholar: Author Only Title Only Author and Title

Essuman, K., Summers, D.W., Sasaki, Y., Mao, X., DiAntonio, A., and Milbrandt, J. (2017). The SARM1 Toll/Interleukin-1 Receptor Domain Possesses Intrinsic NAD(+) Cleavage Activity that Promotes Pathological Axonal Degeneration. Neuron 93, 1334-1343 e1335.
Google Scholar: Author Only Title Only Author and Title

Feinstein, W.P., and Brylinski, M. (2015). Calculating an optimal box size for ligand docking and virtual screening against experimental and predicted binding pockets. J Cheminform 7, 18.
Google Scholar: Author Only Title Only Author and Title

Felsenstein, J. (2009). PHYLIP (phylogeny inference package) version 3.69. (Seattle (WA): Department of Genome Sciences, University of Washington).
Google Scholar: Author Only Title Only Author and Title

Fu, Z.Q., Guo, M., Jeong, B.R., Tian, F., Elthon, T.E., Cerny, R.L., Staiger, D., and Alfano, J.R. (2007). A type III effector ADP-ribosylates RNA-binding proteins and quells plant immunity. Nature 447, 284-288.
Google Scholar: Author Only Title Only Author and Title

Fuchs, E.L., Brutinel, E.D., Klem, E.R., Fehr, A.R., Yahr, T.L., and Wolfgang, M.C. (2010). In vitro and in vivo characterization of the Pseudomonas aeruginosa cyclic AMP (cAMP) phosphodiesterase CpdA, required for cAMP homeostasis and virulence factor regulation. J Bacteriol 192, 2779-2790.
Google Scholar: Author Only Title Only Author and Title

Gallego-Jara, J., Ortega, A., Lozano Terol, G., Sola Martinez, R.A., Canovas Diaz, M., and de Diego Puente, T. (2021). Bacterial Sirtuins Overview: An Open Niche to Explore. Front Microbiol 12, 744416.
Google Scholar: Author Only Title Only Author and Title

Garau, G., Muzzolini, L., Tornaghi, P., and Degano, M. (2010). Active site plasticity revealed from the structure of the enterobacterial N-ribohydrolase RihA bound to a competitive inhibitor. BMC Structural Biology 10.
Google Scholar: Author Only Title Only Author and Title

Gay, N., and Keith, F. (1991). Drosophila Toll and IL-1 receptor. Nature 351, 355-256.
Google Scholar: Author Only Title Only Author and Title

Ghosh, J., and Caparon, M.G. (2006). Specificity of Streptococcus pyogenes NAD(+) glycohydrolase in cytolysin-mediated

translocation. Mol Microbiol 62, 1203-1214.
Google Scholar: Author Only Title Only Author and Title

Gomila, M., Busquets, A., Mulet, M., Garcia-Valdes, E., and Lalucat, J. (2017). Clarification of Taxonomic Status within the Pseudomonas syringae Species Group Based on a Phylogenomic Analysis. Front Microbiol 8, 2422.
Google Scholar: Author Only Title Only Author and Title

Graeff, R., Liu, Q., Kriksunov, I.A., Kotaka, M., Oppenheimer, N., Hao, Q., and Lee, H.C. (2009). Mechanism of cyclizing NAD to cyclic ADP-ribose by ADP-ribosyl cyclase and CD38. J Biol Chem 284, 27629-27636.
Google Scholar: Author Only Title Only Author and Title

Grahnert, A., Grahnert, A., Klein, C., Schilling, E., Wehrhahn, J., and Hauschildt, S. (2011). NAD+: A modulator of immune functions. Innate Immunity 17, 212-233.
Google Scholar: Author Only Title Only Author and Title

Grant, C.E., Bailey, T.L., and Noble, W.S. (2011). FIMO: scanning for occurrences of a given motif. Bioinformatics 27, 1017-1018.
Google Scholar: Author Only Title Only Author and Title

Guangchuang, Y. (2020). Using ggtree to Visualize Data on Tree-Like Structures. Current Protocols in Bioinformatics 69, e96.
Google Scholar: Author Only Title Only Author and Title

Gurevich, A., Saveliev, V., Vyahhi, N., and Tesler, G. (2013). QUAST: quality assessment tool for genome assemblies. Bioinformatics 29, 1072-1075.
Google Scholar: Author Only Title Only Author and Title

Guttman, D.S., Vinatzer, B.A., Sarkar, S.F., Ranall, M.V., Kettler, G., and Greenberg, J.T. (2002). A Functional Screen for the Type III (Hrp) Secretome of the Plant Pathogen Pseudomonas syringae. Science 295, 1722-1725.
Google Scholar: Author Only Title Only Author and Title

Hann, D.R., Dominguez-Ferreras, A., Motyka, V., Dobrev, P.I., Schornack, S., Jehle, A., Felix, G., Chinchilla, D., Rathjen, J.P., and Boller, T. (2014). The Pseudomonas type III effector HopQ1 activates cytokinin signaling and interferes with plant innate immunity. New Phytol 201, 585-598.
Google Scholar: Author Only Title Only Author and Title

Hofer, K., Li, S., Abele, F., Frindert, J., Schlotthauer, J., Grawenhoff, J., Du, J., Patel, D.J., and Jaschke, A. (2016). Structure and function of the bacterial decapping enzyme NudC. Nat Chem Biol 12, 730-734.
Google Scholar: Author Only Title Only Author and Title

Hogan, K.A., Chini, C.C.S., and Chini, E.N. (2019). The Multi-faceted Ecto-enzyme CD38: Roles in Immunomodulation, Cancer, Aging, and Metabolic Diseases. Front Immunol 10, 1187.
Google Scholar: Author Only Title Only Author and Title

Horsefield, S., Burdett, H., Zhang, X., Manik, K.M., Shi, Y., Chen, J., Qi, T., Gilley, J., Lai, J.S., Rank, M.X., et al. (2020). NAD + cleavage activity by animal and plant TIR domains in cell death pathways. Science 365, 793-799.
Google Scholar: Author Only Title Only Author and Title

Huang, S., Jia, A., Song, W., Hessler, G., Meng, Y., Sun, Y., Xu, L., Laessle, H., Jirschitzka, J., Ma, S., et al. (2022). Identification and receptor mechanism of TIR-catalyzed small molecules in plant immunity. BioRxiv.
Google Scholar: Author Only Title Only Author and Title

Irwin, J.J., Tang, K.G., Young, J., Dandarchuluun, C., Wong, B.R., Khurelbaatar, M., Moroz, Y.S., Mayfield, J., and Sayle, R.A. (2020). ZINC20-A Free Ultralarge-Scale Chemical Database for Ligand Discovery. J Chem Inf Model 60, 6065-6073.
Google Scholar: Author Only Title Only Author and Title

Jain, C., Rodriguez-R, L., Phillippy, A.M., Konstantinidis, K.T., and Aluru, S. (2018). High throughput ANI analysis of 90K prokaryotic genomes reveals clear species boundaries. Nat Commun 9, 5114.
Google Scholar: Author Only Title Only Author and Title

Jia, A., Huang, S., Song, W., Wang, J., Meng, Y., Sun, Y., Xu, L., Laessle, H., Jirschitzka, J., Hou, J., et al. (2022). TIR-catalyzed ADP-ribosylation reactions produce signaling molecules for plant immunity. BioRxiv.
Google Scholar: Author Only Title Only Author and Title

Jiang, H., Sherwood, R., Zhang, S., Zhu, X., Liu, Q., Graeff, R., Kriksunov, I.A., Lee, H.C., Hao, Q., and Lin, H. (2013). Identification of ADP-ribosylation sites of CD38 mutants by precursor ion scanning mass spectrometry. Anal Biochem 433, 218-226.
Google Scholar: Author Only Title Only Author and Title

Johanndrees, O., Baggs, E.L., Uhlmann, C., Locci, F., Läßle, H.L., Melkonian, K., Käufer, K., Dongus, J.A., Nakagami, H., Krasileva, K.V., et al. (2021). Differential EDS1 requirement for cell death activities of plant TIR-domain proteins. BioRxiv.
Google Scholar: Author Only Title Only Author and Title

Jones, D.T. (1999). Protein secondary structure prediction based on position-specific scoring matrices. Journal of Molecular

Biology 292, 195-202.
Google Scholar: Author Only Title Only Author and Title

Kazmierczak, B.I., Lebron, M.B., and Murray, T.S. (2006). Analysis of FimX, a phosphodiesterase that governs twitching motility in Pseudomonas aeruginosa. Mol Microbiol 60, 1026-1043.
Google Scholar: Author Only Title Only Author and Title

Kloosterman, A.M., Shelton, K.E., van Wezel, G.P., Medema, M.H., and Mitchell, D.A. (2020). RRE-Finder: a Genome-Mining Tool for Class-Independent RiPP Discovery. mSystems 5, e00267-00220.
Google Scholar: Author Only Title Only Author and Title

Kourelis, J., and van der Hoorn, R.A.L. (2018). Defended to the Nines: 25 Years of Resistance Gene Cloning Identifies Nine Mechanisms for R Protein Function. Plant Cell 30, 285-299.
Google Scholar: Author Only Title Only Author and Title

Krivak, R., and Hoksza, D. (2018). P2Rank: machine learning based tool for rapid and accurate prediction of ligand binding sites from protein structure. J Cheminform 10, 39.
Google Scholar: Author Only Title Only Author and Title

Laemmli, U.K. (1970). Cleavage of structural proteins during the assembly of the head of bacteriophage T4. Nature 227, 680-685.
Google Scholar: Author Only Title Only Author and Title

Lapin, D., Bhandari, D.D., and Parker, J.E. (2020). Origins and Immunity Networking Functions of EDS1 Family Proteins. Annu Rev Phytopathol 58, 253-276.
Google Scholar: Author Only Title Only Author and Title

Leavitt, A., Yirmiya, E., Amitai, G., Lu, A., Garb, J., Morehouse, B.R., Hobbs, S.J., Kranzusch, P.J., and Sorek, R. (2022). Viruses inhibit TIR gcADPR signaling to overcome bacterial defense. BioRxiv.
Google Scholar: Author Only Title Only Author and Title

Lee, H.C., and Zhao, Y.J. (2019). Resolving the topological enigma in Ca(2+) signaling by cyclic ADP-ribose and NAADP. J Biol Chem 294, 19831-19843.
Google Scholar: Author Only Title Only Author and Title

Lenth, R.V. (2022). emmeans: Estimated Marginal Means, aka Least-Squares Means. R package version 1.7.3.
Google Scholar: Author Only Title Only Author and Title

Levy, A., Salas Gonzalez, I., Mittelviefhaus, M., Clingenpeel, S., Herrera Paredes, S., Miao, J., Wang, K., Devescovi, G., Stillman, K., Monteiro, F., et al. (2018). Genomic features of bacterial adaptation to plants. Nat Genet 50, 138-150.
Google Scholar: Author Only Title Only Author and Title

Li, W., Chiang, Y.H., and Coaker, G. (2013). The HopQ1 effector's nucleoside hydrolase-like domain is required for bacterial virulence in arabidopsis and tomato, but not host recognition in tobacco. PLoS One 8, e59684.
Google Scholar: Author Only Title Only Author and Title

Liu, Q., Kriksunov, I.A., Graeff, R., Lee, H.C., and Hao, Q. (2007). Structural basis for formation and hydrolysis of the calcium messenger cyclic ADP-ribose by human CD38. J Biol Chem 282, 5853-5861.
Google Scholar: Author Only Title Only Author and Title

Lo, T., Koulena, N., Seto, D., Guttman, D.S., and Desveaux, D. (2017). The HopF family of Pseudomonas syringae type III secreted effectors. Mol Plant Pathol 18, 457-468.
Google Scholar: Author Only Title Only Author and Title

Ma, S., Lapin, D., Liu, L., Sun, Y., Song, W., Zhang, X., Logemann, E., Yu, D., Wang, J., Jirschitzka, J., et al. (2020). NAD+ cleavage activity by animal and plant TIR domains in cell death pathways. Science 370.
Google Scholar: Author Only Title Only Author and Title

Manik, M.K., Shi, Y., Li, S., Zaydman, M.A., Damaraju, N., Eastman, S., Smith, T.G., Gu, W., Masic, V., Mosaiab, T., et al. (2022). Chemical structures of cyclic ADP ribose (cADPR) isomers and the molecular basis of their production and signaling. BioRxiv.
Google Scholar: Author Only Title Only Author and Title

Menetrey, J., Flatau, G., Boquet, P., Menez, A., and Stura, E.A. (2008). Structural basis for the NAD-hydrolysis mechanism and the ARTT-loop plasticity of C3 exoenzymes. Protein Sci 17, 878-886.
Google Scholar: Author Only Title Only Author and Title

Minh, B.Q., Schmidt, H.A., Chernomor, O., Schrempf, D., Woodhams, M.D., von Haeseler, A., and Lanfear, R. (2020). IQ-TREE 2: New Models and Efficient Methods for Phylogenetic Inference in the Genomic Era. Mol Biol Evol 37, 1530-1534.
Google Scholar: Author Only Title Only Author and Title

Mirdita, M., Schütze, K., Moriwaki, Y., Heo, L., Ovchinnikov, S., and Steinegger, M. (2022). ColabFold - Making protein folding accessible to all. BioRxiv.

Google Scholar: Author Only Title Only Author and Title

Munshi, C., Aarhus, R., Graeff, R., Walseth, T.F., Levitt, D., and Lee, H.C. (2000). Identification of the enzymatic active site of CD38 by site-directed mutagenesis. J Biol Chem 275, 21566-21571.
Google Scholar: Author Only Title Only Author and Title

O'Boyle, N., Banck, M., James, C., Morley, C., Vandermeersch, T., and Hutchison, G. (2011). Open Babel: An open chemical toolbox. Journal of Cheminformatics 3.
Google Scholar: Author Only Title Only Author and Title

Ofir, G., Herbst, E., Baroz, M., Cohen, D., Millman, A., Doron, S., Tal, N., Malheiro, D.B.A., Malitsky, S., Amitai, G., et al. (2021). Antiviral activity of bacterial TIR domains via immune signalling molecules. Nature 600, 116-120.
Google Scholar: Author Only Title Only Author and Title

Pandit, S.B., and Skolnick, J. (2008). Fr-TM-align: a new protein structural alignment method based on fragment alignments and the TM-score. BMC Bioinformatics 9, 531.
Google Scholar: Author Only Title Only Author and Title

Paradis, E., and Schliep, K. (2019). ape 5.0: an environment for modern phylogenetics and evolutionary analyses in R. Bioinformatics 35, 526-528.
Google Scholar: Author Only Title Only Author and Title

Parks, D.H., Imelfort, M., Skennerton, C.T., Hugenholtz, P., and Tyson, G.W. (2015). CheckM: assessing the quality of microbial genomes recovered from isolates, single cells, and metagenomes. Genome Res 25, 1043-1055.
Google Scholar: Author Only Title Only Author and Title

Pereira, J., and Alva, V. (2021). How do I get the most out of my protein sequence using bioinformatics tools? Acta Crystallogr D Struct Biol 77, 1116-1126.
Google Scholar: Author Only Title Only Author and Title

Petersen, C., and Moller, L.B. (2001). The RihA, RihB, and RihC ribonucleoside hydrolases of Escherichia coli. Substrate specificity, gene expression, and regulation. J Biol Chem 276, 884-894.
Google Scholar: Author Only Title Only Author and Title

Petnicki-Ocwieja, T., Schneider, D.J., Tam, V.C., Chancey, S.T., Shan, L., Jamir, Y., Schechter, L.M., Janes, M.D., Buell, C.R., Tang, X., et al. (2002). Genomewide identification of proteins secreted by the Hrp type III protein secretion system of Pseudomonas syringae pv. tomato DC3000. Proc Natl Acad Sci U S A 99, 7652-7657.
Google Scholar: Author Only Title Only Author and Title

R.Core.Team (2020). R: A language and environment for statistical computing. (Vienna, Austria: R Foundation for Statistical Computing,).
Google Scholar: Author Only Title Only Author and Title

Ramakrishnan, L., Muller-Steffner, H., Bosc, C., Vacquier, V.D., Schuber, F., Moutin, M.J., Dale, L., and Patel, S. (2010). A single residue in a novel ADP-ribosyl cyclase controls production of the calcium-mobilizing messengers cyclic ADP-ribose and nicotinic acid adenine dinucleotide phosphate. J Biol Chem 285, 19900-19909.
Google Scholar: Author Only Title Only Author and Title

Salentin, S., Schreiber, S., Haupt, V.J., Adasme, M.F., and Schroeder, M. (2015). PLIP: fully automated protein-ligand interaction profiler. Nucleic Acids Res 43, W443-447.
Google Scholar: Author Only Title Only Author and Title

Sanders, B.D., Jackson, B., and Marmorstein, R. (2010). Structural basis for sirtuin function: what we know and what we don't. Biochim Biophys Acta 1804, 1604-1616.
Google Scholar: Author Only Title Only Author and Title

Schliep, K.P. (2011). phangorn: phylogenetic analysis in R. Bioinformatics 27, 592-593.
Google Scholar: Author Only Title Only Author and Title

Schreiber, K.J., Chau-Ly, I.J., and Lewis, J.D. (2021). What the Wild Things Do: Mechanisms of Plant Host Manipulation by Bacterial Type III-Secreted Effector Proteins. Microorganisms 9.
Google Scholar: Author Only Title Only Author and Title

Seemann, T. (2014). Prokka: rapid prokaryotic genome annotation. Bioinformatics 30, 2068-2069.
Google Scholar: Author Only Title Only Author and Title

Shi, Y., Kerry, P.S., Nanson, J.D., Bosanac, T., Sasaki, Y., Krauss, R., Saikot, F.K., Adams, S.E., Mosaiab, T., Masic, V., et al. (2022). Structural basis of SARM1 activation, substrate recognition, and inhibition by small molecules. Mol Cell.
Google Scholar: Author Only Title Only Author and Title

Soding, J., Biegert, A., and Lupas, A.N. (2005). The HHpred interactive server for protein homology detection and structure

prediction. Nucleic Acids Res 33, W244-248.
Google Scholar: Author Only Title Only Author and Title

Srouji, J.R., Xu, A., Park, A., Kirsch, J.F., and Brenner, S.E. (2017). The evolution of function within the Nudix homology clan. Proteins 85, 775-811.
Google Scholar: Author Only Title Only Author and Title

Stivala, A., Wybrow, M., Wirth, A., Whisstock, J.C., and Stuckey, P.J. (2011). Automatic generation of protein structure cartoons with Pro-origami. Bioinformatics 27, 3315-3316.
Google Scholar: Author Only Title Only Author and Title

Sun, Y., Li, P., Shen, D., Wei, Q., He, J., and Lu, Y. (2019). The Ralstonia solanacearum effector RipN suppresses plant PAMP-triggered immunity, localizes to the endoplasmic reticulum and nucleus, and alters the NADH/NAD(+) ratio in Arabidopsis. Mol Plant Pathol 20, 533-546.
Google Scholar: Author Only Title Only Author and Title

Takamura-Enya, T., Watanabe, M., Totsuka, Y., Kanazawa, T., Matsushima-Hibiya, Y., Koyama, K., Sugimura, T., and Wakabayashi, K. (2001). Mono(ADP-ribosyl)ation of 2'-deoxyguanosine residue in DNA by an apoptosis-inducing protein, pierisin-1, from cabbage butterfly. Proc Natl Acad Sci U S A 98, 12414-12419.
Google Scholar: Author Only Title Only Author and Title

Thompson, J., Higgins, D., and Gibson, T. (1994). CLUSTAL W: improving the sensitivity of progressive multiple sequence alignment through sequence weighting, position-specific gap penalties and weight matrix choice. Nucleic Acids Res 22, 4673-4680.
Google Scholar: Author Only Title Only Author and Title

Tohgo, A., Munakata, H., Takasawa, S., Nata, K., Akiyama, T., Hayashi, N., and Okamoto, H. (1997). Lysine 129 of CD38 (ADP-ribosyl cyclase/cyclic ADP-ribose hydrolase) participates in the binding of ATP to inhibit the cyclic ADP-ribose hydrolase. J Biol Chem 272, 3879-3882.
Google Scholar: Author Only Title Only Author and Title

Toshchakov, V.Y., and Neuwald, A.F. (2020). A survey of TIR domain sequence and structure divergence. Immunogenetics 72, 181-203.
Google Scholar: Author Only Title Only Author and Title

Turko, I.V., Francis, S.H., and Corbin, J.D. (1998). Potential roles of conserved amino acids in the catalytic domain of the cGMP-binding cGMP-specific phosphodiesterase. J Biol Chem 273, 6460-6466.
Google Scholar: Author Only Title Only Author and Title

Ve, T., Williams, S.J., and Kobe, B. (2015). Structure and function of Toll/interleukin-1 receptor/resistance protein (TIR) domains. Apoptosis 20, 250-261.
Google Scholar: Author Only Title Only Author and Title

Vinatzer, B.A., Jelenska, J., and Greenberg, J.T. (2005). Bioinformatics Correctly Identifies Many Type III Secretion Substrates in the Plant Pathogen Pseudomonas syringae and the Biocontrol Isolate P. fluorescens SBW25. MPMI 18, 877-888.
Google Scholar: Author Only Title Only Author and Title

Wan, L., Essuman, K., Anderson, R.G., Sasaki, Y., Monteiro, F., Chung, E.H., Osborne Nishimura, E., DiAntonio, A., Milbrandt, J., Dangl, J.L., et al. (2019). TIR domains of plant immune receptors are NAD(+)-cleaving enzymes that promote cell death. Science 365, 799-803.
Google Scholar: Author Only Title Only Author and Title

Ward, J.L., Forcat, S., Beckmann, M., Bennett, M., Miller, S.J., Baker, J.M., Hawkins, N.D., Vermeer, C.P., Lu, C., Lin, W., et al. (2010). The metabolic transition during disease following infection of Arabidopsis thaliana by Pseudomonas syringae pv. tomato. Plant J 63, 443-457.
Google Scholar: Author Only Title Only Author and Title

Wei, H.L., Chakravarthy, S., Mathieu, J., Helmann, T.C., Stodghill, P., Swingle, B., Martin, G.B., and Collmer, A. (2015). Pseudomonas syringae pv. tomato DC3000 Type III Secretion Effector Polymutants Reveal an Interplay between HopAD1 and AvrPtoB. Cell Host Microbe 17, 752-762.
Google Scholar: Author Only Title Only Author and Title

Wickham, H. (2007). Reshaping Data with the reshape Package. Journal of Statistical Software 21, 1-20.
Google Scholar: Author Only Title Only Author and Title

Wickham, H. (2016). ggplot2: Elegant Graphics for Data Analysis (New York: Springer-Verlag).
Google Scholar: Author Only Title Only Author and Title

Wolters, V., Rosche, A., Bauche, A., Kulow, F., Harneit, A., Fliegert, R., and Guse, A.H. (2019). NAD binding by human CD38 analyzed by Trp189 fluorescence. Biochim Biophys Acta Mol Cell Res 1866, 1189-1196.

Google Scholar: Author Only Title Only Author and Title

Xin, X.F., Kvitko, B., and He, S.Y. (2018). Pseudomonas syringae: what it takes to be a pathogen. Nat Rev Microbiol 16, 316-328.
Google Scholar: Author Only Title Only Author and Title

Young, J.M. (2010). Taxonomy of Pseudomonas syringae. Journal of Plant Pathology 92, S1.5-S1.14.
Google Scholar: Author Only Title Only Author and Title

Yu, D., Song, W., Tan, E.Y.J., Liu, L., Cao, Y., Jirschitzka, J., Li, E., Logemann, E., Xu, C., Huang, S., et al. (2022). TIR domains of plant immune receptors are 2',3'-cAMP/cGMP synthetases mediating cell death. Cell.
Google Scholar: Author Only Title Only Author and Title

Yuan, H., and Marmorstein, R. (2012). Structural basis for sirtuin activity and inhibition. J Biol Chem 287, 42428-42435.
Google Scholar: Author Only Title Only Author and Title

Yuan, J., and He, S.Y. (1996). The Pseudomonas syringae Hrp Regulation and Secretion System Controls the Production and Secretion of Multiple Extracellular Proteins. J Bacteriol 178, 6399-6402.
Google Scholar: Author Only Title Only Author and Title

Zhou, H., Morgan, R.M., Guttman, S., and Ma, W. (2009). Allelic Variants of the Pseudomonas syringae Type III Effector HopZ1 Are Differentially Recognized by Plant Resistance Systems. MPMI 22, 176-189.
Google Scholar: Author Only Title Only Author and Title